Geoscientific
Model Development

Impact of physical parameterizations on wind simulation with WRF V3.9.1.1 under stable conditions at planetary boundary layer gray-zone resolution: a case study over the coastal regions of North China

Entao Yu[1,2], **Rui Bai**[1,3], **Xia Chen**[4,5], **and Lifang Shao**[4]

[1]Nansen-Zhu International Research Centre, Institute of Atmospheric Physics, Chinese Academy of Sciences, Beijing, China
[2]Collaborative Innovation Center on Forecast and Evaluation of Meteorological Disasters (CIC-FEMD),
Nanjing University of Information Science & Technology, Nanjing, China
[3]University of Chinese Academy of Science (UCAS), Beijing, China
[4]Hebei Climate Center, Shijiazhuang, China
[5]Hebei Key Laboratory for Meteorology and Eco-environment, Shijiazhuang, China

Correspondence: Entao Yu (yuet@mail.iap.ac.cn) and Xia Chen (chenxia1218@sina.com)

Abstract. Reliable simulation of wind fields under stable weather conditions is vital for preventing air pollution. In this study, we investigate how different physical parameterizations impact simulated near-surface wind at 10 m height over the coastal regions of North China using the Weather Research and Forecasting (WRF) model with a horizontal grid spacing of 0.5 km. We performed 640 simulations using combinations of 10 planetary boundary layer (PBL), 16 microphysics (MP), and four shortwave–longwave radiation (SW–LW) schemes. Model performance is evaluated using measurements from 105 weather station observations. The results show that the WRF model can reproduce the temporal variation of wind speed in a reasonable way. The simulated wind speed is most sensitive to the PBL schemes, followed by SW–LW schemes and MP schemes. Among all PBL schemes, the MYJ scheme shows the best temporal correlation with the observed wind speed, while the Yonsei University (YSU) scheme has the lowest model bias. Dudhia–RRTM and MYDM7 show the best model performances out of all SW–LW and MP schemes, respectively, and the interactions among schemes also have large influences on wind simulation. Further investigation indicates that model sensitivity is also impacted by ocean proximity and elevation. For example, for coastal stations, MYNN shows the best correlation with observations among all PBL schemes, while God-

dard shows the smallest bias of SW–LW schemes; these results are different from those of inland stations. In general, according to the bias metrics, WRF simulates wind speed less accurately for inland stations compared to coastal stations, and the model performance tends to degrade with increasing elevation. The WRF model shows worse performance in simulating wind direction under stable conditions over the study area, with lower correlation scores compared to wind speed. Our results indicate the role parameterizations play in wind simulation under stable weather conditions and provide a valuable reference for further research in the study area and nearby regions.

1 Introduction

Megacities that experience rapid urbanization and economic development also commonly suffer from a simultaneous decline in air quality (Ulpiani, 2021). For example, many haze events have been reported in the Beijing, Tianjin, and Hebei regions of North China over the past few decades. Haze-related weather and associated high concentrations of fine particulate matter have negative impacts on public health and the environment (Wang and Mauzerall, 2006). These events

can significantly disrupt economic growth, as demonstrated by the severe haze events that occurred over North China in January 2013 (Zhang et al., 2014, 2015; Cai et al., 2017). The haze events are most frequent in boreal winter and are closely related to local weather conditions with low wind speeds (Li et al., 2015; Wang et al., 2021). Projections of future climate change suggest that global temperatures and weather conditions conducive to severe haze will increase, affecting North China (Cai et al., 2017). However, numerical models often show a large bias in wind prediction over China (X. Gao et al., 2016; Zhao et al., 2016; Pan et al., 2021), and thus it is crucial to improve wind prediction under stable weather conditions in order to minimize associated economic losses and environmental impacts.

In recent years, numerical models have been used extensively to study and forecast the weather and climate over China, as they have high spatial and temporal resolutions and employ sophisticated physical parameterization schemes that can reproduce atmospheric and land surface processes (Wang et al., 2011; Zhou et al., 2019; Kong et al., 2022). However, studies mostly focus on temperature or precipitation, and only a few have attempted to simulate winds over China (Li et al., 2019; Xia et al., 2019; Pan et al., 2021). Meanwhile, numerical models inherently involve many sources of uncertainty, as they cannot resolve all processes in the real world; instead, parameterizations are needed to represent the effect of key physical processes, such as radiative transfer, turbulent mixing, and moist convection that occur at the sub-grid scale. Different physical parameterization schemes depict natural phenomena to different degrees of accuracy, and choosing appropriate combinations is important, as it can strongly influence model results (Yu et al., 2011; Gómez-Navarro et al., 2015; Stegehuis et al., 2015; X. Gao et al., 2016; Yang et al., 2017; Taraphdar et al., 2021).

The impact of the planetary boundary layer (PBL) scheme on wind simulation has been studied for many years, as the PBL scheme plays a critical role in modulating mass, energy, and moisture fluxes between the land and atmosphere, which in turn influences the simulation of low-level temperatures, cloud formation, and wind fields (Jiménez and Dudhia, 2012; Gómez-Navarro et al., 2015; Gonçalves-Ageitos et al., 2015; Falasca et al., 2021; Gholami et al., 2021). Many studies indicate an overestimation of wind speed in WRF simulations with different PBL schemes (Jiménez and Dudhia, 2012; Carvalho et al., 2014a, b; Pan et al., 2021; Gholami et al., 2021; Dzebre and Adaramola, 2020). For example, Gómez-Navarro et al. (2015) investigate the sensitivity of the WRF model to the PBL scheme by simulating wind storms over complex terrain at a horizontal grid spacing of 2 km. In that study, the WRF model is configured with the Mellor–Yamada–Janjic (MYJ) scheme and overestimates wind speed by up to 100 %; however, the bias is significantly reduced when the non-local scheme developed at Yonsei University (YSU) is used instead. The YSU scheme also shows good model skill in simulating winds over the

Iberian Peninsula, Persian Gulf, Tyrrhenian coast, and western Argentina (Jiménez and Dudhia, 2012; Puliafito et al., 2015; Falasca et al., 2021; Gholami et al., 2021). Other studies suggest that MYNN and ACM2 are more appropriate for wind simulations (Carvalho et al., 2014b; Chang et al., 2015; Prieto-Herráez et al., 2021; Rybchuk et al., 2021).

The performance of wind simulation is also influenced by the choice of cloud microphysics (MP) parameterizations. Cloud microphysical processes, such as moisture evaporation and condensation, can change thermodynamic and dynamic interactions in the atmosphere (Rajeevan et al., 2010; Cheng et al., 2013; Santos-Alamillos et al., 2013; Li et al., 2020) and then affect the vertical distribution of heat and wind fields close to the surface.

Another factor influencing wind simulation is the choice of radiation parameterizations, which include shortwave radiation and longwave radiation (SW–LW) schemes. Differences in surface radiation intensities can generate thermal contrasts in regions with complex topography, which in turn affect local and low-level wind distribution patterns (Santos-Alamillos et al., 2013).

The combinations of physical parameterizations are also vital to wind simulation, as the processes of atmosphere–land interactions, radiation transport, and moist convection interact and may amplify the uncertainties in wind prediction. The impact of parameterization scheme combinations on WRF performance has been investigated in previous studies (Santos-Alamillos et al., 2013; Fernández-González et al., 2018), and Fernández-González et al. (2018) report that there is no single combination of schemes that performs best during all weather conditions. Most of the aforementioned studies considered a small number of parameterization schemes. To our knowledge, the sensitivity of parameterizations to wind simulation has not been explored in a systematic way in China. In this study, we systematically evaluate the performance of a large number of parameterization combinations, including PBL, MP, and SW–LW schemes. The investigation is conducted using the WRF model at a grid spacing of 0.5 km, which belongs to the PBL "gray zone" resolution that is too fine to utilize mesoscale turbulence parameterizations and too coarse for large-eddy-simulation (LES) schemes to resolve turbulent eddies (Shin and Hong, 2015; Honnert et al., 2016). Our main objective is to identify a set of configurations of the WRF model that can best reproduce wind fields under stable weather conditions over North China, which experienced many haze events during the past few years. This study addresses the following research themes: (1) quantify the sensitivity of wind simulation to different parameterizations under stable weather conditions and (2) refine optimized configurations with the best performance in reproducing winds under stable weather conditions over North China. These results would provide a valuable evaluation of WRF performance using a large number of simulations with different physical parameterizations and be helpful in the wind

and air quality forecasts in the study area and other coastal regions of China under stable weather conditions.

2 Data and methods

2.1 The stable weather event in 2019

The study area is located in the central section of the "Bohai Economic Rim", which is bordered to the southeast by the Bohai Sea and to the northwest by the Yan Mountains (Fig. 1a). This region traditionally hosts heavy industry and manufacturing businesses and is a significant region of economic growth and development in North China (Song et al., 2020; Zhao et al., 2020). Air quality in this area has declined over the past decades, and the frequency of winter haze events has increased due to increased pollutant emissions and favorable stable weather conditions with lower wind speed (M. Gao et al., 2016; Cai et al., 2017). For instance, during the heavy fog and haze event over eastern China in January 2013, an anomalous southerly wind in the lower troposphere caused by the weak East Asian winter monsoon weakened the synoptic forcing and extent of vertical mixing in the atmosphere, thus increasing the stability of air in the boundary layer and the local concentration of hazes (Zhang et al., 2014).

During 11–15 January 2019, a severe haze event occurred in the study area, the peak $PM_{2.5}$ and PM_{10} concentrations exceeded 279 and 357 $\mu g\,m^{-3}$ in Tangshan city, and 282 and 358 $\mu g\,m^{-3}$ in Qinhuangdao city, respectively, the locations of the two cities can be found in Fig. 1. Figure 2 depicts the distribution of geopotential height at 500 hPa, surface winds at 10 m and total cloud fraction from the ERA5 dataset (Hersbach et al., 2020) during the study period. A weak high-pressure system persisted from 11 to 14 January 2019 over the study area, with the geopotential height at 500 hPa of about 5400 gpm, at the surface level (10 m), weak southwest winds occurred at the south side of the study area on 11, 12 and 14 January 2019. The surface wind speeds over the study area were weaker than 5 $m\,s^{-1}$ during the first 4 d of the study period , and then the geopotential height decreased and strong northwesterly winds occurred over the study area on 15 January 2019. Although there were slight differences between ERA5 and satellite products (e.g., CLARA, Karlsson et al., 2021), both datasets indicated higher cloud fraction on 11 and 14 January 2019, while for the rest of the time, the cloud fraction was low. This stable weather event is used to investigate the impact of physical parameterizations of the WRF model.

2.2 Model configurations

The WRF model (version 3.9.1.1) with the advanced research WRF (ARW) core is used in this study, which is a non-hydrostatic atmospheric model with terrain-following vertical coordinates (Skamarock et al., 2008). The simulations

Table 1. List of default parameterization schemes for the simulation of outer domains (D01 and D02).

Parameterizations	D01	D02
Microphysics	SBU	SBU
Planetary boundary layer	Shin–Hong	Shin–Hong
Shortwave radiation	CAM	CAM
Longwave radiation	CAM	CAM
Culumus	Modified Tiedtke (Tiedtke, 1989)	None
Land surface	Noah-MP	Noah-MP

contain three one-way nested domains with grid spacings of 8, 2, and 0.5 km for D01, D02, and D03, respectively (Fig. 1b). The computational domains are based on Lambert conformal conic projection centered at 38.5° N and 120° E, with 360×480, 381×381, and 341×421 grid points for D01, D02, and D03, respectively. The evaluations are based on the innermost domain, which covers the coastal and surrounding regions of North China (Fig. 1a). The simulation domain has 65 vertical levels, and the eta values for the first 10 levels are 0.996, 0.988, 0.978, 0.966, 0.956, 0.946, 0.933, 0.923, 0.912, and 0.901: this ensures that sufficient model levels exist within the PBL at any time.

The ERA5 reanalysis dataset, which has a horizontal resolution of 0.25° and 38 vertical levels, is used to provide the initial and boundary conditions for WRF simulations. The WRF model is initialized at 00:00 UTC (08:00 in local time) on 9 January 2019, with the first 40 h treated as the spin-up period. Firstly, the default physical parameterization schemes (Table 1) are applied in the WRF simulation for the outer two domains (D01 and D02), and then the output of D02 is used to drive inner-domain simulations with different combinations of PBL, MP, and SW–LW schemes (see Sect. 2.3). This approach helps to isolate the impacts of parameterization within the inner domain from changes in boundary forcing (Yang et al., 2017). All simulations apply the Noah land surface model with multi-parameterization options (Noah-MP, Yang et al., 2011; Niu et al., 2011) as the land surface parameterization scheme. The lateral boundary conditions and sea surface temperature are updated every 3 h using the ERA5 reanalysis data, and the frequency of wind retrieved from WRF output is hourly, which matches the frequency of observations in the study area.

2.3 Experimental design

The WRF model contains different parameterization schemes that represent different physical processes. Further, every scheme in the model has many parameters, such that a model can range from being simple and efficient to be sophisticated and computationally costly. In this study, a systematic evaluation of parameterizations is achieved by considering
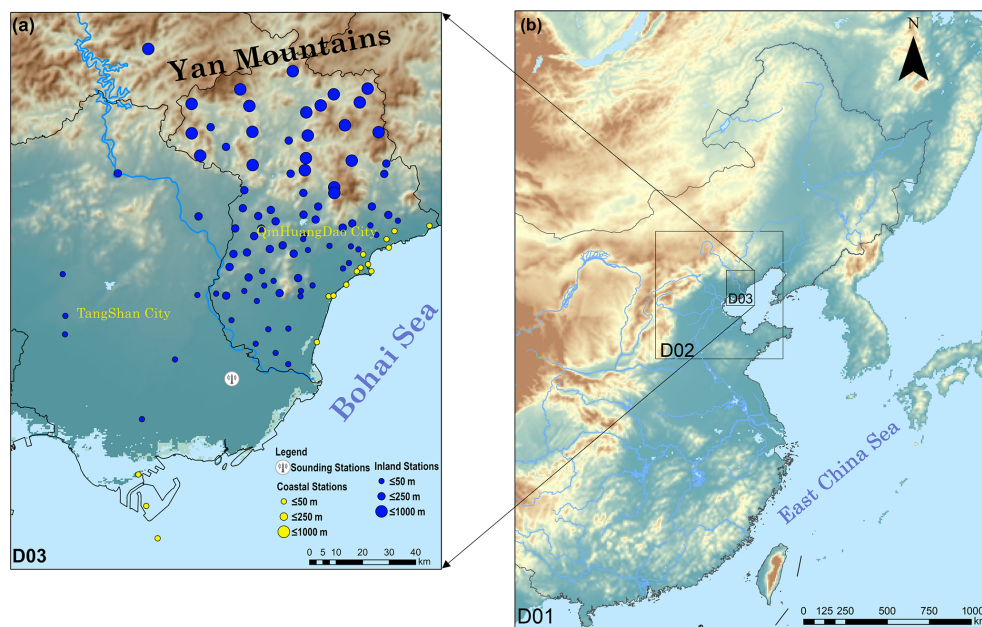
Figure 1. Map showing the **(a)** study area and **(b)** WRF nested domains (D01–D03). Solid yellow and blue circles in panel **(a)** represent coastal (16 stations in total) and inland stations (89 stations in total), the sizes of the circles represent the station elevations, and the white circle represents the sounding station.
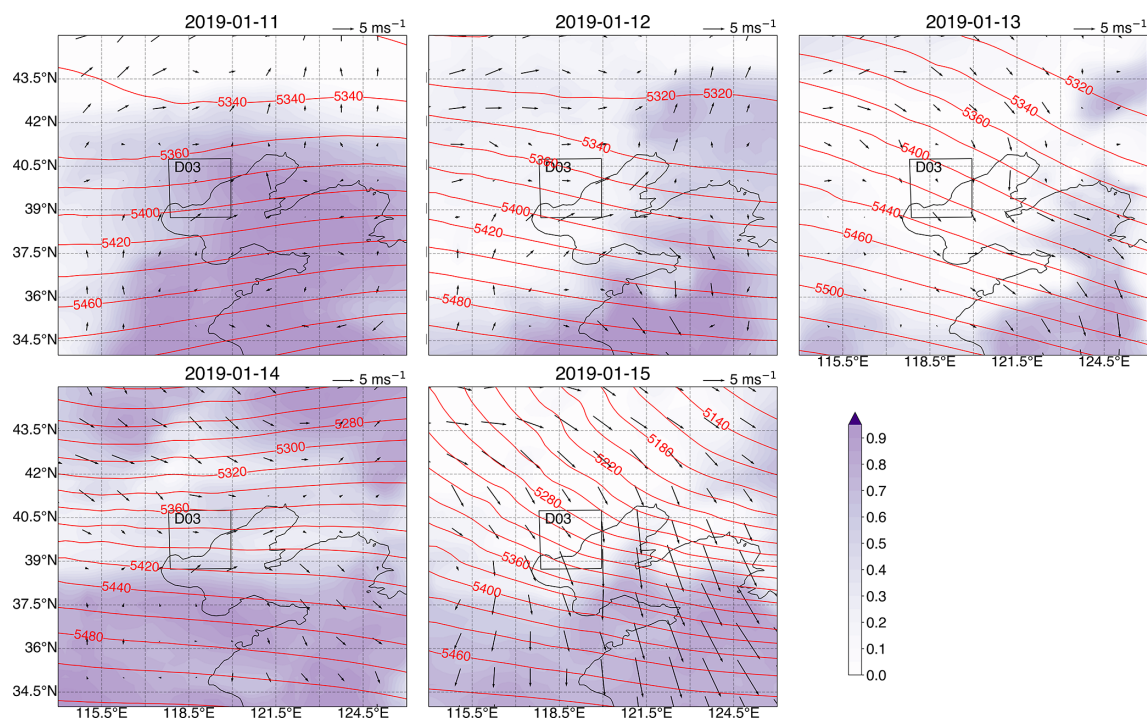

Figure 2. The daily averaged geopotential height (contour lines, units: gpm) at 500 hPa, total cloud fraction (shading), and surface winds at 10 m (vectors, units: m s^{-1}) from ERA5 during 11–15 January 2019; the box indicates the D03 domain in Fig. 1.

10 PBL, 16 MP, and 4 LW-SW schemes, which produce 640 (i.e., $10 \times 16 \times 4$) combinations in total.

The parameterization schemes investigated in this study are listed in Table 2. As the horizontal grid spacing of 0.5 km is within the PBL gray zone resolution, both PBL and LES assumptions are imperfect: we test both the PBL and LES schemes in this study. For the LES configuration, the 1.5-order turbulence kinetic energy closure model is used to parameterize motion at the sub-grid scale (Deardorff, 1985). For the YSU scheme, topographic correction for surface winds is included to represent extra drag from sub-grid topography and enhanced flow at hilltops (Jiménez and Dudhia, 2012). The option for top-down mixing driven by radiative cooling is also turned on during the integration. For the rest of the PBL schemes, the default configurations are chosen. The atmospheric surface layer (SL) is the lowest part of the atmospheric boundary layer, of which the parameterizations are used to quantify surface heat and moisture fluxes in the land surface model and surface stress in the PBL schemes. In the current generation of WRF, the SL schemes are tied to the PBL schemes. In this study, the ETA, QNSE, MYNN, Pleim-Xiu, and TEMF SL schemes are chosen for the PBL schemes of MYJ, QNSE, MYNN, ACM2, and TEMF, respectively. The revised MM5 scheme (Jimenez et al., 2012) is used for the remaining PBL schemes.

Sixteen MP schemes are applied in this study (Table 2), Lin, WSM3, WSM5, ETA, WSM6, Goddard, SBU, and NSSL1 schemes are the single-moment bulk microphysical scheme, which predicts only the mixing ratios of hydrometeors (i.e., cloud ice, snow, graupel, rain, and cloud water) by assuming particle size distributions. The other eight schemes (Thompson, MYDM7, Morrison, CMA, WDM6, NSSL2, ThompsonAA and P3) use a double-moment approach, predicting not only mixing ratios of hydrometeors, but also number concentrations. Among them, two types of hydrometeors are included in WSM3 (cloud water and rain), three types of hydrometeors are included in ETA (cloud water, rain, and snow) and P3 (cloud water, rain, and ice), four types of hydrometeors are included in WSM5 and SBU (cloud water, rain, ice, and snow), five types of hydrometeors are included in Lin, WSM6, Goddard, Thompson, Morrison, CAM, WDM6 and ThompsonAA (cloud water, rain, ice, snow, and graupel), six types of hydrometeors are included in MYDM7, NSSL1, and NSSL2 (cloud water, rain, ice, snow, graupel, and hail).

Four SW–LW combinations are applied in this study (Table 2), Dudhia is a simple and efficient shortwave radiation scheme for clouds and clear-sky absorption and scattering; RRTM provides efficient look-up tables for longwave radiation; CAM SW–LW schemes are derived from the CAM3 model used in CCSM3 and allow modeling of aerosols and trace gases. RRTMG is a scheme that utilizes Monte Carlo independent column approximation (MCICA) method of random cloud overlap.

2.4 Observational data and evaluation metrics

Observations from weather stations across the study region are used to evaluate the performance of the model. These stations are operated by the China Meteorology Administration (CMA) and report wind speed and direction at an altitude of 10 m. In this study, we use 2 min averaged wind speed at hourly frequency. All data are screened before analysis in order to remove stations with data showing spurious jumps (e.g., wind speed jumps to $0 \, \text{m s}^{-1}$ due to the frozen sensor). After this filtering, 105 out of 132 weather stations (Fig. 1a) remained, including 89 inland stations and 16 coastal stations. The results of WRF are directly compared with observations at each weather station, which is achieved by using the model result that is geographically closest to the weather station under consideration. Although some errors are introduced when performing these comparisons, they are systematic and shared by all simulations and therefore have minor effects on the evaluation of model performances.

Several metrics are employed for evaluating the performance of each model configuration, including the Pearson correlation coefficient (CORR), BIAS, root mean square error (RMSE), and Taylor skill score (T). CORR is a measure of the strength and direction of the linear relationship between simulation and observation, BIAS is a measure of the mean difference between simulation and observation, and RMSE is the square root of the average of the set of squared differences between simulation and observation, and thus each of these scores gives a partial view of the model performance.

They are defined as follows:

$$
\text{CORR} = \frac{\sum_{i=1}^{N}(M_i - \overline{M})(O_i - \overline{O})}{\sqrt{\sum_{i=1}^{N}(M_i - \overline{M})^2 \cdot \sum_{i=1}^{N}(O_i - \overline{O})^2}},
$$

$$
\text{BIAS} = \frac{1}{N}\sum_{i=1}^{N}(M_i - O_i)
$$

$$
\text{RMSE} = \sqrt{\frac{1}{N}\sum_{i=1}^{N}(M_i - O_i)^2},
$$

$$
T = \frac{2(1 + \text{CORR})}{\left(\text{SD} + \frac{1}{\text{SD}}\right)^2}.
$$

Here, M is the value of the model output, O is the value of the observation, N is the number of observations, and SD is the ratio of simulated-to-observed standard deviation. A higher Taylor skill score indicates a more accurate simulation (Gan et al., 2019), while higher CORR, lower BIAS, and RMSE scores indicate better model simulations.

The difference in wind direction was calculated as follows.

$$
\Delta = \begin{cases} M - O, & \text{when } |M - O| \le 180° \\ (M - O)\left(1 - \dfrac{360}{|M - O|}\right), & \text{when } |M - O| > 180° \end{cases}
$$

Table 2. List of microphysics (MP), planetary boundary layer (PBL), and shortwave–longwave radiation (SW–LW) schemes investigated in the 640 simulations; schemes that share rows are not specifically assigned to each other (except for SW–LW).

	MP	PBL	SW	LW
1	Purdue Lin (Lin; Chen and Sun, 2002)	LES (Mirocha et al., 2010)	Dudhia (Dudhia, 1989)	RRTM (Mlawer et al., 1997)
2	WRF single-moment three-class (WSM3; Hong et al., 2004)	Yonsei University (YSU; Hong et al., 2006)	CAM (Collins et al., 2004)	CAM (Collins et al., 2004)
3	WRF single-moment five-class (WSM5; Hong et al., 2004)	Mellor–Yamada–Janjic (MYJ; Janjić, 1994; Mesinger, 1993)	RRTMG (Iacono et al., 2008)	RRTMG (Iacono et al., 2008)
4	ETA Ferrier (ETA, Rogers et al., 2001)	Quasi-normal-scale elimination (QNSE; Sukoriansky et al., 2005)	Goddard (Matsui et al., 2020)	Goddard (Matsui et al., 2020)
5	WRF single-moment six-class (WSM6; Hong and Lim, 2006)	Mellor–Yamada Nakanishi Niino 2.5 level TKE (MYNN; Nakanishi and Niino, 2009)		
6	Goddard (Tao et al., 1989)	Asymmetric convection model 2 (ACM2; Pleim, 2007)		
7	Thompson (Thompson et al., 2008)	Bougeault–Lacarrere (BouLac; Bougeault and Lacarrere, 1989)		
8	Milbrandt–Yau double-moment seven-class (MYDM7; Milbrandt and Yau, 2005)	University of Washington (UW; Bretherton and Park, 2009)		
9	Morrison double moment (Morrison; Morrison et al., 2009)	TEMF (Angevine et al., 2010)		
10	CAM double-moment five-class (CAM; Eaton, 2011)	Shin–Hong scale-aware (Shin–Hong, Shin and Hong, 2015)		
11	Stony-Brook University (SBU; Lin and Colle, 2011)			
12	WRF double-moment six-class (WDM6; Lim and Hong, 2010)			
13	NSSL double moment (NSSL2; Mansell et al., 2010)			
14	NSSL single-moment seven-class (NSSL1, Mansell et al., 2010)			
15	Aerosol-aware Thompson (ThompsonAA; Thompson and Eidhammer, 2014)			
16	P3 (Morrison and Milbrandt, 2015)			

The correlation between simulated and measured angles is determined by a circular correlation coefficient, and the mean of the angular is calculated using the vector notation approach. The circular correlation coefficient is calculated as follows.

$$\text{CORR} = \frac{\sum_{i=1}^{N} \sin(\alpha_i - \overline{\alpha}) \sin(\beta_i - \overline{\beta})}{\sqrt{\sum_{i=1}^{N} \sin^2(\alpha_i - \overline{\alpha}) \sin^2(\beta_i - \overline{\beta})}}$$

Here, α and β are simulated and observed wind direction angles, respectively.

3   Results

3.1   Impacts of physical parameterizations

3.1.1   PBL

Figure 3a shows the time series of observed wind speed in local time. Model wind speeds are shown for different PBL

schemes averaged over all other parameterization types. The WRF model generally reproduces the temporal variation of observed wind speed in the study area with exaggeration; in particular, the shift from low to high wind speed on 14 January 2019 is reproduced by all schemes except for QNSE, with which the wind speed change is considerably larger than with all other schemes during the simulation period. Almost all the PBL schemes overestimate wind speed by $1\,\text{m}\,\text{s}^{-1}$; however, for the QNSE scheme, the largest overestimation exceeds $10\,\text{m}\,\text{s}^{-1}$ during the daytime on 11 and 15 January 2019. The difference between simulation and observation is lower during 11–13 January 2019 using the LES scheme, while YSU is more similar to the measurements during 14–15 January 2019. In addition, the spread within the PBL schemes is larger on 15 January 2019, partly due to the high wind speed ($> 4\,\text{m}\,\text{s}^{-1}$) or the general error growth in the model.

The statistics of CORR, BIAS, and RMSE are illustrated in Fig. 3b–d. MYJ shows the best CORR score of 0.96;
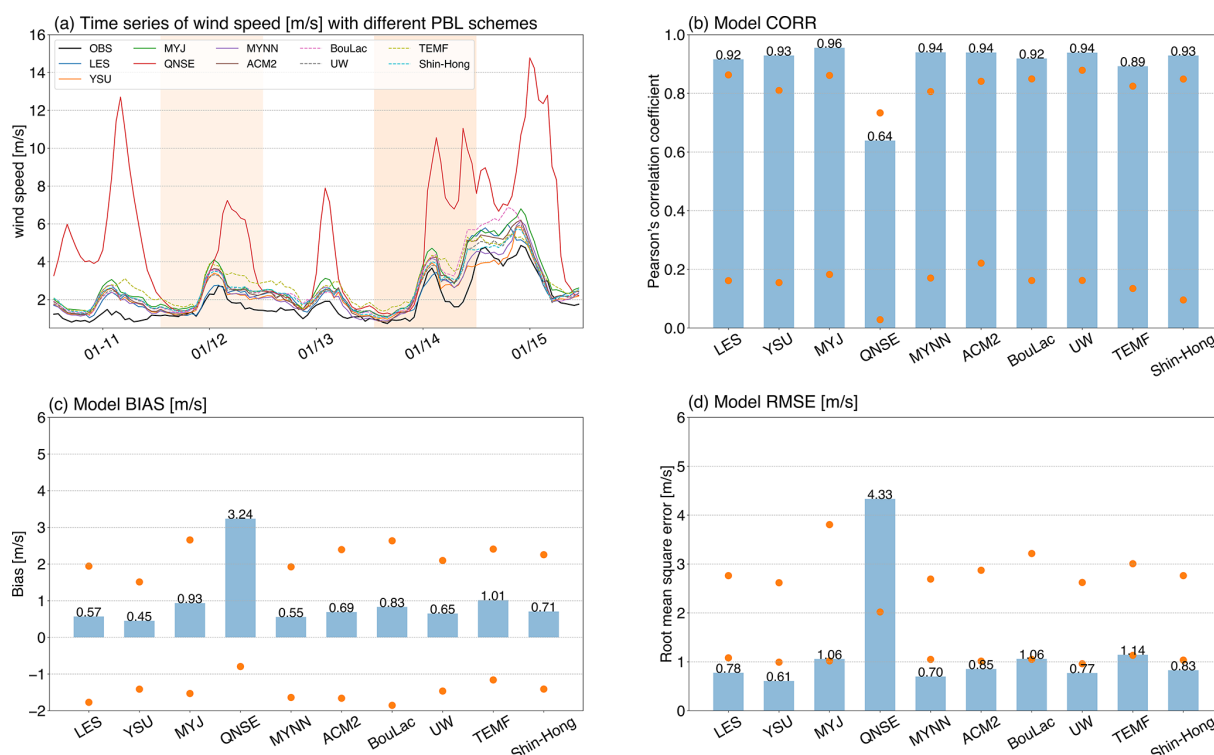
Figure 3. (a) Time series of observed and simulated wind speeds $(\mathrm{m\,s^{-1}})$ and the corresponding statistics of **(b)** CORR, **(c)**, BIAS, and **(d)** RMSE for the PBL schemes. In panel **(a)**, the frequency of wind speed is hourly, and the tick marks on the x axis indicate 12:00 LT of that day, for each PBL scheme, and the average is calculated over the 105 stations and then over all the simulations with that scheme. The dots in panels **(b)**–**(d)** represent the range across the stations, for each station, and the metrics are calculated by averaging all the simulations with the specific PBL scheme.

MYNN, ACM2, and UW are the next best according to this verification score. YSU is the best scheme in terms of BIAS and RMSE, with the values of 0.45 and 0.61 m s^{-1} followed by MYNN (0.55 and 0.70 m s^{-1}). The ranges of statistic scores across the 105 stations are also illustrated in Fig. 3, for the schemes except for QNSE, and the range of CORR is 0.18–0.88, the range of BIAS is −2.10–2.91 m s^{-1}, and the range of RMSE is 0.79–3.85 m s^{-1}. Further comparison indicates that the CORR scores for individual stations are lower than the ensemble means, and the BIAS and RMSE are larger than the ensemble means. For the QNSE scheme, the maximum BIAS and RMSE scores for individual stations exceed 10 and 16 m s^{-1}, indicating that it has problems in reproducing wind speed under stable conditions over the study area.

Figure 4 shows the wind roses during 11–15 January 2019 from observations and simulations with different PBL schemes as well as the statistic scores. Observations indicate that, during the study period, wind is mostly from a southwesterly-to-northwesterly direction (225–330°), while simulations with different PBL schemes produce primarily southwesterly wind (200–270°), indicating an anticlockwise bias of wind direction over the study area under stable conditions. Further comparison indicates that all PBL schemes strongly overestimate the speed of northerly wind compared

to the observations, which may be the main cause of positive bias in wind speed (Fig. 3). The CORR scores of wind direction (0.42–0.59) are notably lower than those of wind speed, indicating the degraded performance of WRF in wind direction simulation. LES shows the best CORR score of 0.59, while TEMF shows the best BIAS and RMSE scores of −11.33 and 56.19°. Considering the large model bias in wind speed, simulations with the QNSE scheme (64 in total) are omitted from further investigation in order that these anomalous data do not affect our overall analysis.

3.1.2 MP

Figure 5 shows the time series of wind speed from the observations and simulations with different MP schemes. The simulations are similar, especially during 14–15 January 2019. The spread among simulations with different MP schemes is smaller than that with different PBL schemes, indicating that wind speed is less sensitive to the MP schemes. The CORR scores are very similar for all the MP schemes at a precision of 0.01, while MYDM7 is the best scheme according to the BIAS and RMSE scores, followed by P3 and ETA. The range of statistical scores across the stations is similar within dif-
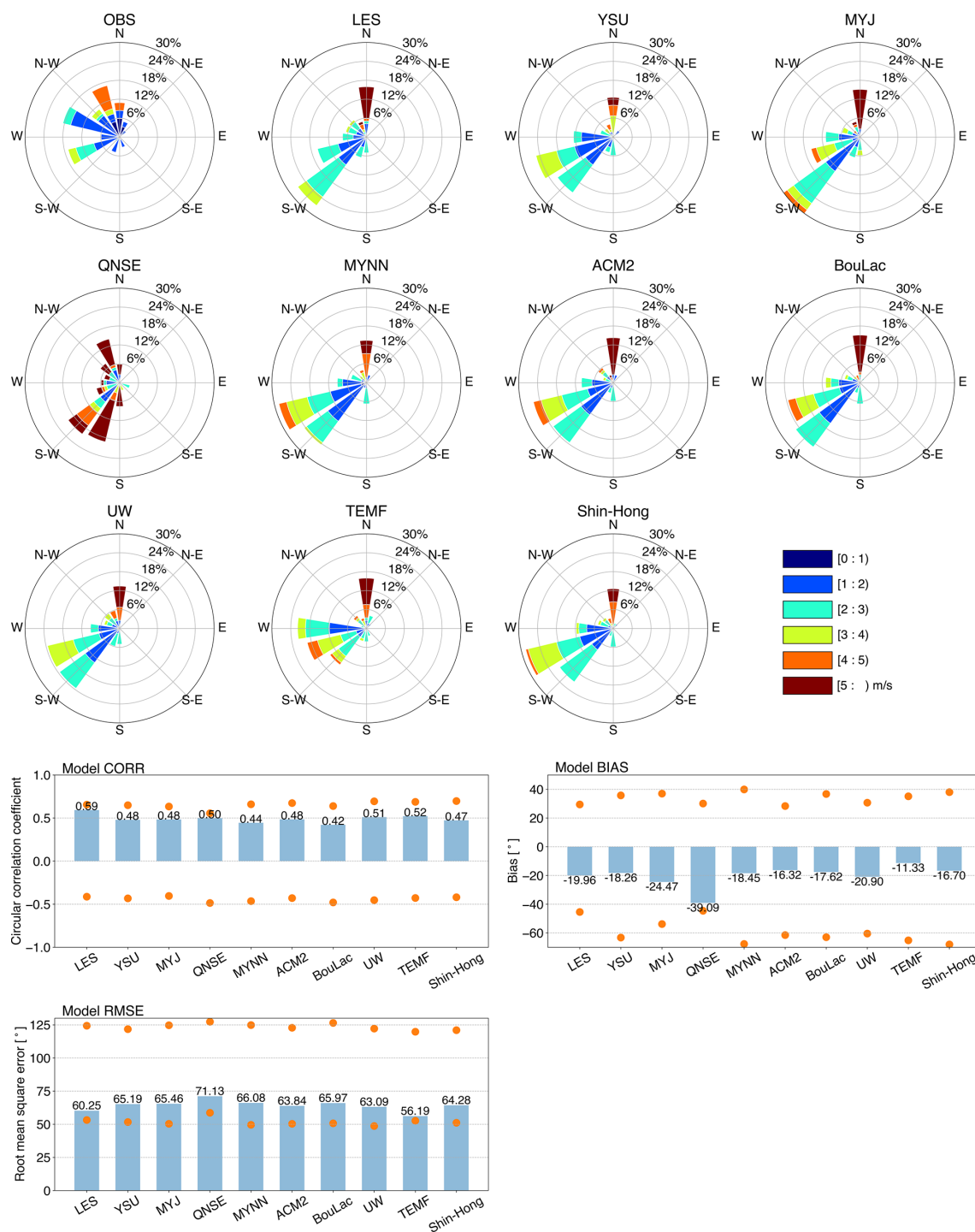
Figure 4. The wind rose charts for the PBL schemes during 11–15 January 2019 averaged over the stations and the corresponding scores of CORR, BIAS, and RMSE; for each wind rose chart, the circles represent the relative frequency (%), and the colors represent wind speed (m s^{-1}).
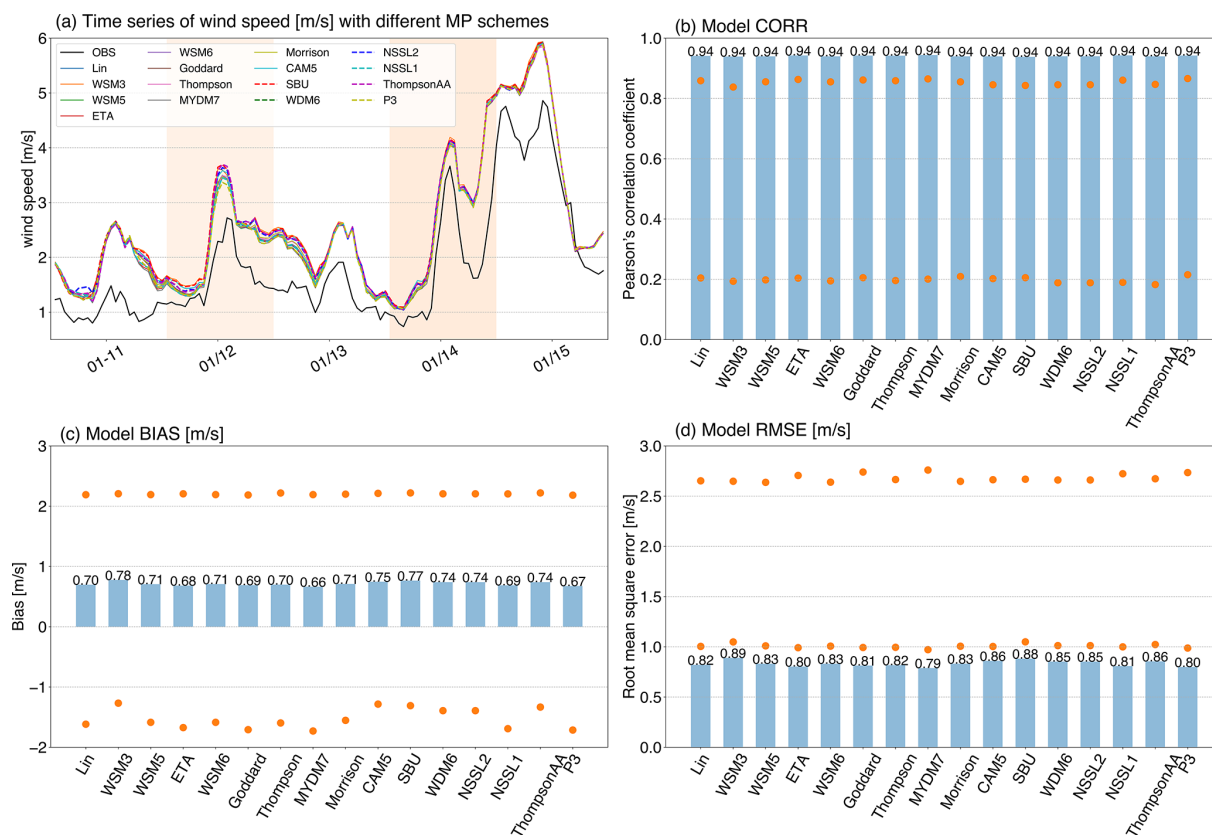
Figure 5. Same as Fig. 3 but for the MP schemes.

ferent MP schemes, which provides a further indication of the low sensitivity of wind speed to MP schemes.

The sensitivity of wind direction to the MP schemes is also low, as the wind roses from simulations with different MP schemes are very similar (Fig. 6). WDM6, NSSL2 and ThompsonAA show the best CORR score of 0.52, followed by Thompson and CAM5. Meanwhile, WSM3 is the best scheme according to the BIAS score, and ThompsonAA is the best scheme according to the RMSE score.

3.1.3 Radiation

Figure 7 shows the time series of observed and simulated wind speed, the ensemble spread among different SW–LW schemes is larger than that with different MP schemes, but smaller than that with different PBL schemes, which indicates that simulated wind speed is more sensitive to the SW–LW schemes than the MP schemes and less sensitive to the PBL schemes. RRTMG and CAM show a larger overestimation than Dudhia–RRTM and Goddard at daytime peaks. The CORR scores are very similar for the SW–LW schemes at a precision of 0.01, and Dudhia–RRTM is the best scheme according to BIAS and RMSE scores, followed by Goddard.

Figure 8 shows the wind roses during 11–15 January 2019 from simulations with different SW–LW schemes and the

corresponding statistic scores. In simulations, wind is mostly from the southwest direction during the study period, which is different from the observation. According to the CORR score, Dudhia–RRTM is the best scheme with the highest value (0.55); meanwhile, the RRTMG scheme shows the best BIAS of $-15.69°$, and Dudhia–RRTM shows the best RMSE of $61.13°$. As wind direction is more variable but less important under stable conditions with weak wind speed, the subsequent investigations mainly focus on wind speed.

3.1.4 Interactions among parameterization schemes

Interactions among physical parameterizations also play an important role in wind simulation. Since it is not possible to show all possible combinations of PBL, MP, and SW–LW schemes in this study, the results of interactions between PBL and SW–LW schemes are selected as examples, which are illustrated in Fig. 9. The MP schemes used in the simulations are MYDM7 and P3, given that they show better performance in earlier investigations (see Sect. 3.1.2), and thus for each MP scheme, a total of 36 simulations (excluding QNSE) is illustrated. For wind speed simulations, the combination of MYJ and Dudhia–RRTM shows the best CORR, while the combination of YSU and Dudhia–RRTM ranks best according to BIAS and RMSE scores. For wind direction
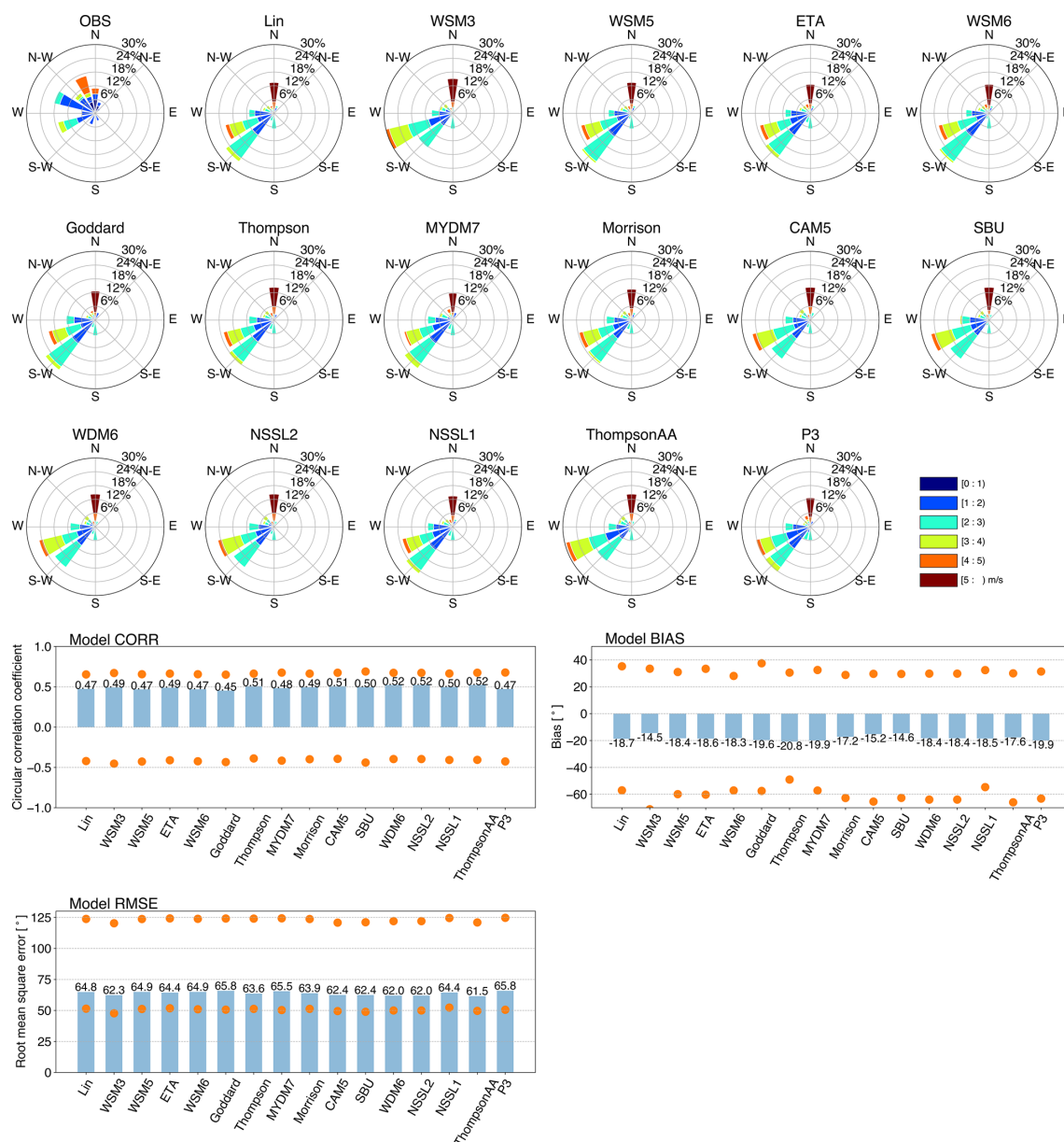
Figure 6. Same as Fig. 4, but for the MP schemes.

simulations, the combination of LES and Dudhia–RRTM shows the best CORR. According to BIAS and RMSE scores, the combination of TEMF and Dudhia–RRTM ranks best in MYDM7 case, and the combination of TEMP and RRTMG ranks best in P3 case.

Overall, for BIAS and RMSE scores of wind speed, within each PBL scheme, the same SW–LW group ranks best, and within each SW–LW group, the same PBL scheme ranks best. For example, no matter which SW–LW group, YSU is always the best, which indicate the good performance of YSU. However, it is worth noting that YSU shows pretty low BIAS ($< 0.4\,\mathrm{m\,s^{-1}}$) and RMSE ($< 0.6\,\mathrm{m\,s^{-1}}$) scores only when combined with the Dudhia–RRTM or Goddard

schemes, when it is combined with RRTMG schemes, the BIAS and RMSE scores increase a lot. For the wind direction simulation, the pattern is different from that of wind speed. For example, for BIAS and RMSE scores, the best PBL scheme depends on the choice of SW–LW schemes, which indicates the influence of scheme interaction on model performance in wind direction simulations.

3.1.5 WRF configurations with the best individual performance

To determine the WRF configuration with the best individual performance, Taylor skill scores are calculated for wind
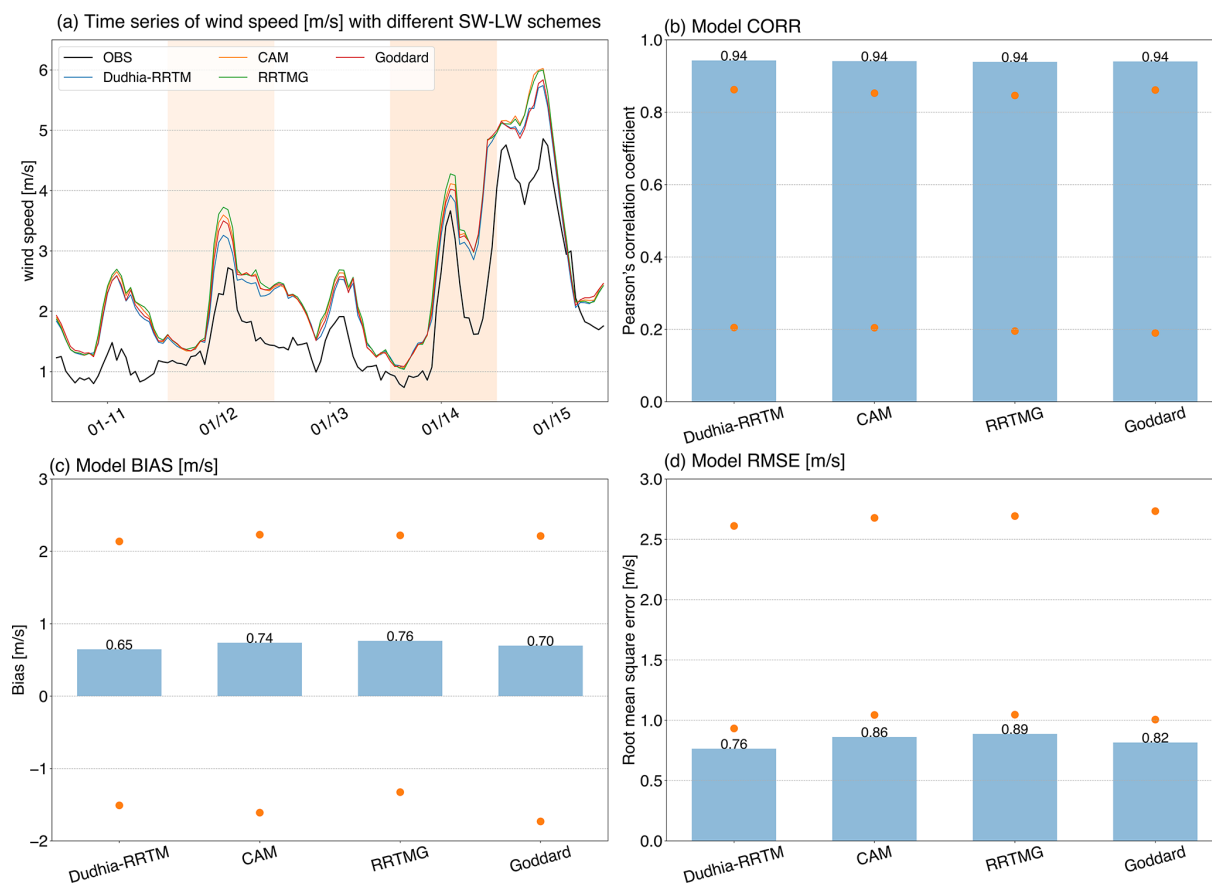
Figure 7. Same as Fig. 3, but for the radiation schemes.

speed within all simulations, the scores range from 0.2 to 1.0, with the best 10 WRF configurations having similar scores of about 1.0. The time series and statistics are illustrated in Fig. 10. The best 10 configurations have in common that they use the same PBL and SW–LW schemes, namely YSU and Dudhia–RRTM. This indicates a large impact of PBL and SW–LW on wind speed simulation compared with MP schemes and highlights the best performance of YSU and Dudhia–RRTM. Since Taylor skill score considers both correlation and standard deviation, the best scheme (i.e., WDM6) is not the scheme that has the best CORR (i.e., Goddard), BIAS (i.e., MYDM7 and ETA), or RMSE (i.e., Goddard, NSSL1, MYDM7 and ETA). In fact, there is no scheme that has all the best scores of CORR, BIAS and RMSE. Thus, model ensemble is needed to improve the performance. Figure 10 also illustrates the ensemble of different number of simulations, as well as a super ensemble of all 576 simulations (excluding QNSE). The result indicates that ensemble mean of four simulations with WDM6, Goddard, NSSL1 and MYDM7 MP schemes shows the best BIAS and RMSE scores. For the time series of wind speed (Fig. 10a), the spread of ENS(4) is significantly lower than that of ENS(576), and ENS(4) shows lower bias

compared to ENS(576). According to the statistic scores, ENS(4) reduces model bias by approximately half compared to ENS(576), at the same time, the best individual schemes (NSSL1, MYDM7, P3 and ETA) can also reduce the bias by $\sim 50\%$. It is worth to mention that the best CORR score of ENS(576) is also result of single model simulation with Goddard MP scheme. At the same time, the best BIAS score ($0.33\,\mathrm{m\,s^{-1}}$) is result of the single model simulation with MYDM7 or ETA, and the best RMSE score ($0.52\,\mathrm{m\,s^{-1}}$) is result of either the single model simulation with Goddard, NSSL1, MYDM7, or the ensemble using the three, four, or five best simulations.

3.2 Performance dependency on ocean proximity and elevation

Land surface conditions can affect the partitioning of sensible and latent heat fluxes, which impacts local low-level circulation patterns and wind distribution (Yu et al., 2013; Barlage et al., 2016). The weather stations in the study region were classified into different groups according to the ocean proximity and elevation.
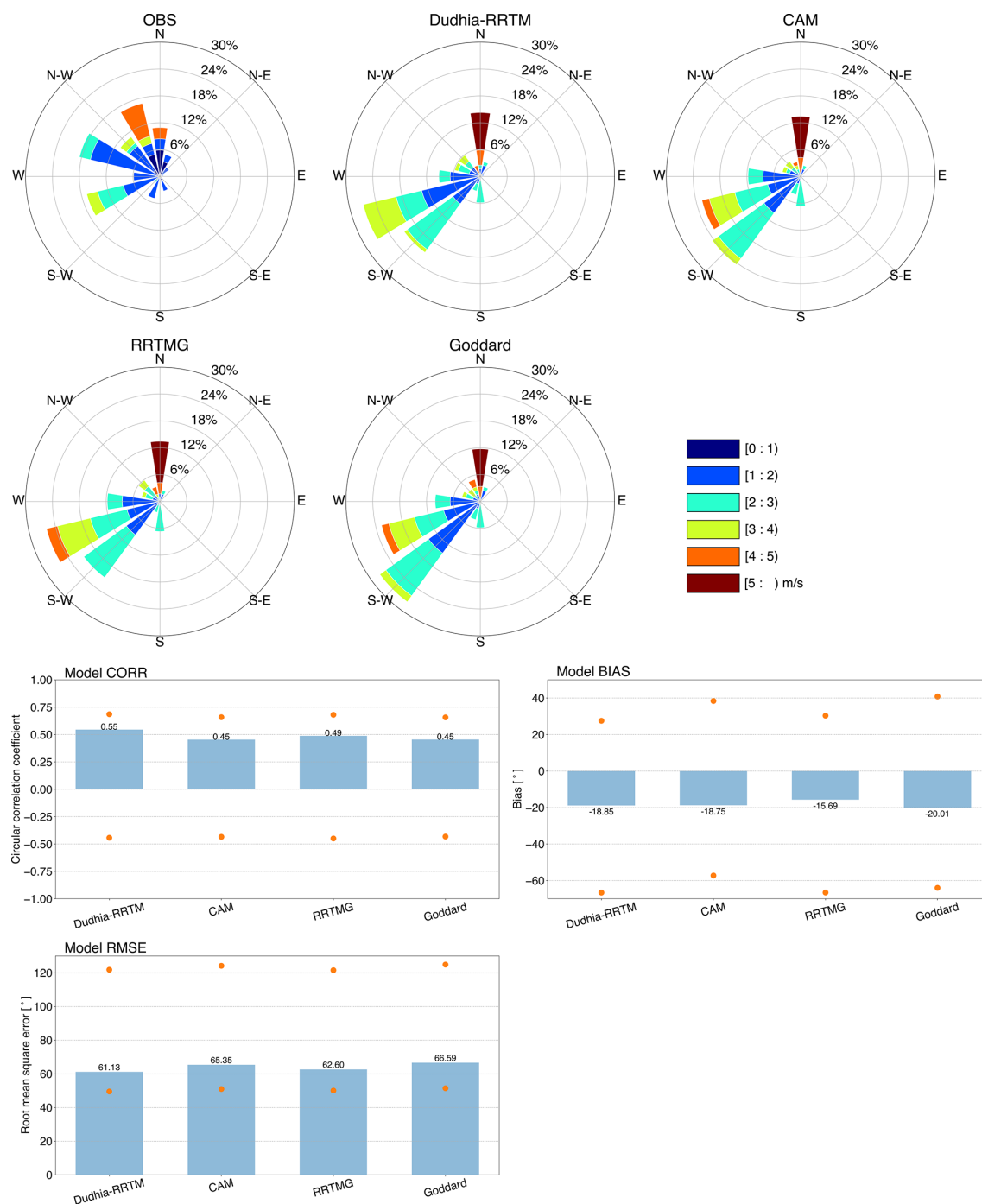
Figure 8. Same as Fig. 4, but for the radiation schemes.

3.2.1   Ocean proximity

Figure 11 compares the results of wind speed for coastal stations (closer than 5 km from the shoreline, 16 stations in total) and inland stations (over 5 km from the shoreline, 89 stations in total), the locations of these stations are shown in Fig. 1a. For both coastal and inland stations, the ensemble spread is the largest among the PBL schemes, followed by SW–LW and MP schemes, which is consistent with the results of the previous analysis in this study. WRF reproduces the time series of wind speed reasonably, with a larger overestimation for inland stations. The ensemble spread is larger for coastal stations compared with inland stations. As such, in addition to physical parameterizations, model performance is also influenced by ocean proximity.
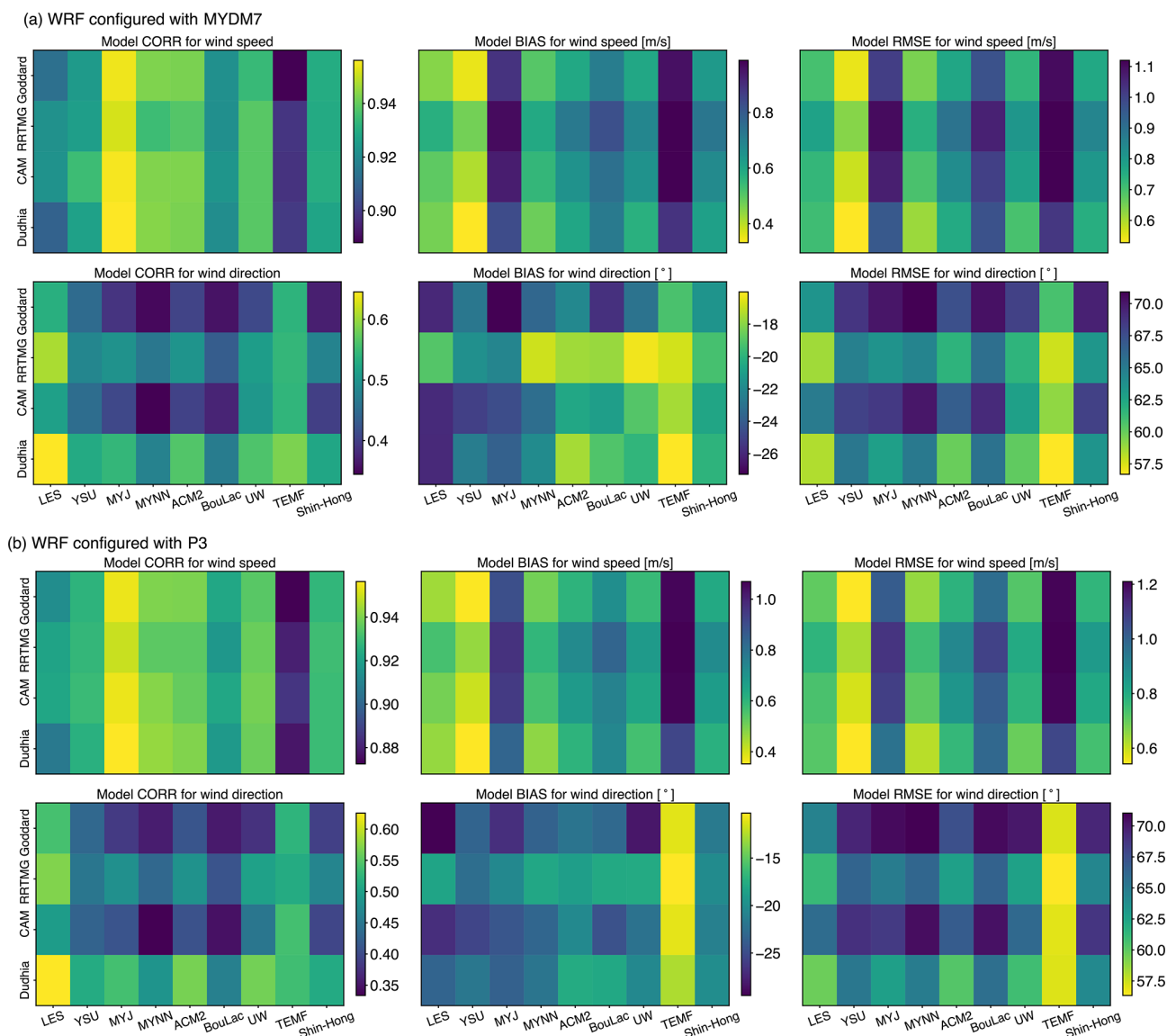
Figure 9. Statistic scores (CORR, BIAS and RMSE) for wind speed and direction for different combinations of PBL and SW–LW schemes, the MP schemes used in panels **(a)** and **(b)** are MYDM7 and P3, respectively. Dudhia represents Dudhia–RRTM SW–LW schemes in all the subplots.

The statistical scores are also illustrated in Fig. 11, the CORR scores are consistently lower for coastal stations compared to inland stations, and the BIAS scores are generally worse for the inland stations. Thus, the model performance tends to degrade for the inland stations according to the BIAS scores.

Our comparison indicates that the parameterization schemes with the best performance for inland stations are generally consistent with those of previous investigations for all the stations in this study, as most of the stations are inland stations (89 out of 105 stations). However, for coastal stations, the results are different. For instance, MYNN shows the best CORR score among the PBL schemes, while LES

(YSU) shows the best BIAS (RMSE) score. For the SW–LW schemes, Goddard shows the best CORR, BIAS, and RMSE, while Dudhia–RRTM ranks worst according to the CORR score.

3.2.2 Elevation

Figure 12 shows the comparison for stations with different elevation (e.g., < 50 m, 51 stations in total; > 50 and < 250 m, 36 stations in total; > 250 m, 19 stations in total). Observation shows that peak wind speed decreases with increasing elevation during the study period; for example, the peak observed wind speed of high-elevation stations (> 250 m) is $1.5 \, \mathrm{m \, s^{-1}}$, slower than that of low-elevation stations ($<$
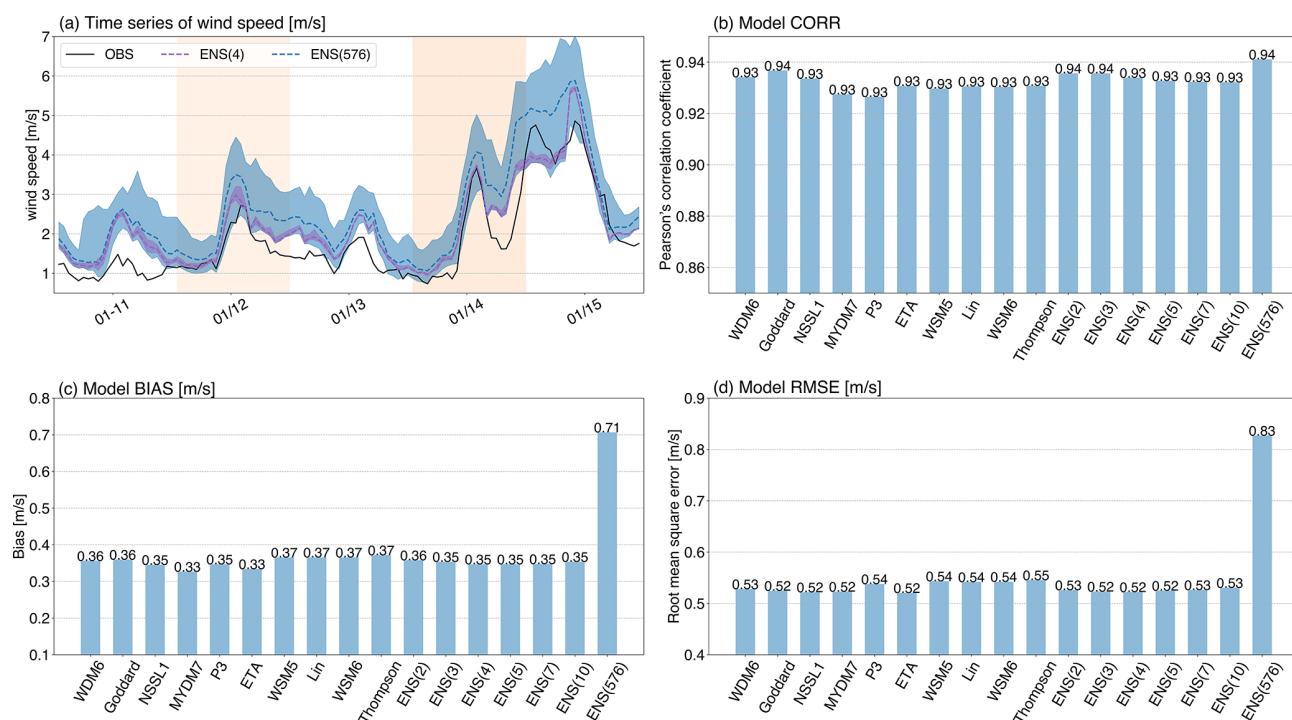
Figure 10. (a) Time series of wind speed ($\mathrm{m\,s^{-1}}$) from observation and different ensembles, and **(b)** CORR, **(c)** BIAS and **(d)** RMSE scores for the best 10 simulations along with different ensembles. The shadings in **(a)** represent the spread for ENS(4) and ENS(576). As the best 10 simulations use the same PBL (YSU) and SW–LW (Dudhia–RRTM) schemes, only the MP schemes are labeled in the figure.

50 m). However, the peak simulated wind speed is generally similar for stations with different elevations, which bring larger model errors for the high-elevation stations. Further investigations are needed to reveal the underlying mechanisms for lower wind speeds of high-elevation stations and the mismatch between observations and model simulations. As shown by the statistical scores, for all PBL, MP, and SW–LW schemes, CORR generally decreases with increasing elevation, while BIAS and RMSE scores increase with elevation, and thus the evaluation metrics tend to degrade with increasing elevation under stable conditions over the study area. For different parameterization types, the scheme with the best performance is generally similar, with different elevations; e.g., for PBL schemes, MYJ is always the best at all elevation categories according to CORR, and YSU always ranks best according to the BIAS and RMSE scores.

3.3 Comparison of simulations with different model performances and the effects of other model options

In order to evaluate atmospheric properties that are crucial for air quality under stable conditions and to investigate what drives the differences in wind speed, we compare the simulated wind field from the simulation with the best Taylor skill score (i.e., using the YSU, Dudhia–RRTM, and WDM6 schemes) and the station observations; meanwhile, the same

simulation but with the QNSE PBL scheme (i.e., using the QNSE, Dudhia–RRTM, and WDM6 schemes) is used for comparison between the simulations with good and poor performances. In addition, the impacts of the land surface model, surface layer scheme, and different options in the YSU scheme are also investigated in this section.

3.3.1 Spatial distribution of the wind field

Figure 13 compares the spatial distribution of observed and simulated wind fields during the study period, and we choose 14:00 LT as an example. The simulation with the best Taylor skill score is referred to as YSU, and the simulation using the QNSE PBL scheme is referred to as QNSE. YSU generally reproduces the wind field in the study area, especially in terms of wind speed. For example, the observed wind speed is lower on 13 January 2019, with values lower than $2\,\mathrm{m\,s^{-1}}$ for many stations, while on 15 January 2019, the observed wind speed is higher than $4\,\mathrm{m\,s^{-1}}$ for most stations. In the simulation using YSU, wind speed is about $2\,\mathrm{m\,s^{-1}}$ on 13 January 2019 and is higher than $4\,\mathrm{m\,s^{-1}}$ on 15 January 2019 over the study area, which is similar to the observation. By contrast, simulation with QNSE fails to reproduce the distribution of wind speed and shows strong overestimation, especially over the mountain areas of the study area; for example, the peak wind speed in simulation with QNSE exceeds $20\,\mathrm{m\,s^{-1}}$ on 15 January 2019, which is more than 5 times
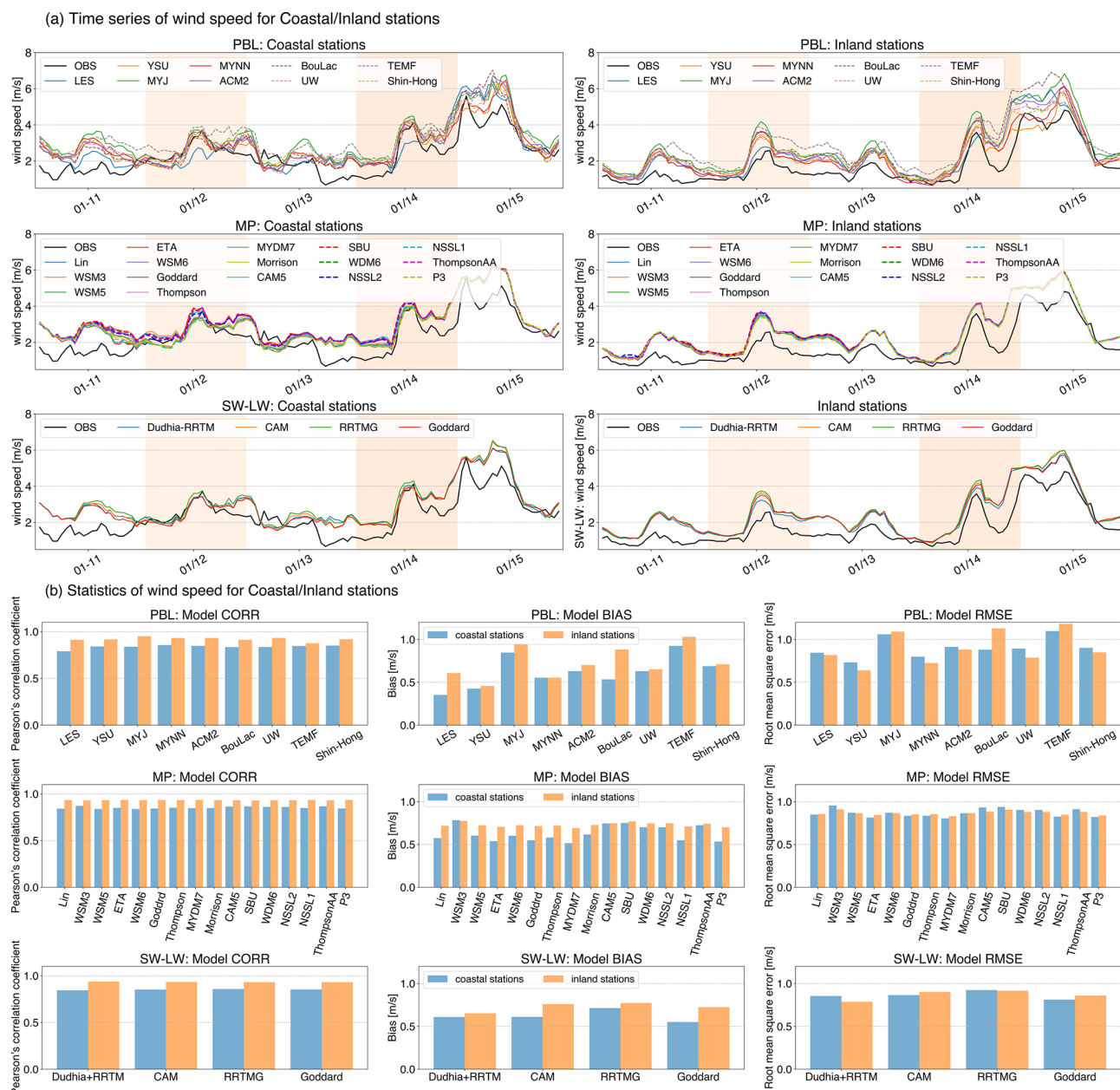
Figure 11. Comparison of simulated wind speeds between the coastal and inland stations shown in Fig. 1a as well as the corresponding statistical scores.

greater than the observation. This overestimation is consistent with the large positive bias in previous investigations of Fig. 3. For the wind direction simulation, YSU shows degraded performance compared to wind speed and generally fails to reproduce the wind direction distribution for most of the stations, which is also the case for QNSE.

3.3.2 Vertical profile of wind speed

Figure 14 shows the observed and simulated vertical profiles of wind speed at 08:00 and 20:00 LT during the study pe-

riod, and the location of the sounding station is illustrated in Fig. 1. YSU reproduces the vertical structure of wind speed reasonably; for example, within the low levels below 2.5 km, the simulated wind speed from the YSU scheme is similar to the observation, with model bias lower than $2.5\,\mathrm{m\,s^{-1}}$ in most cases. Meanwhile, QNSE shows a worse performance in reproducing the vertical structure of wind speed, with a large model bias compared to YSU. QNSE overestimates the wind speed by almost $20\,\mathrm{m\,s^{-1}}$ at 20:00 LT, 11 January 2019, and by $30\,\mathrm{m\,s^{-1}}$ at 20:00 LT, 12 January 2019. It is interesting to note that, at 08:00 LT, the simulations using QNSE
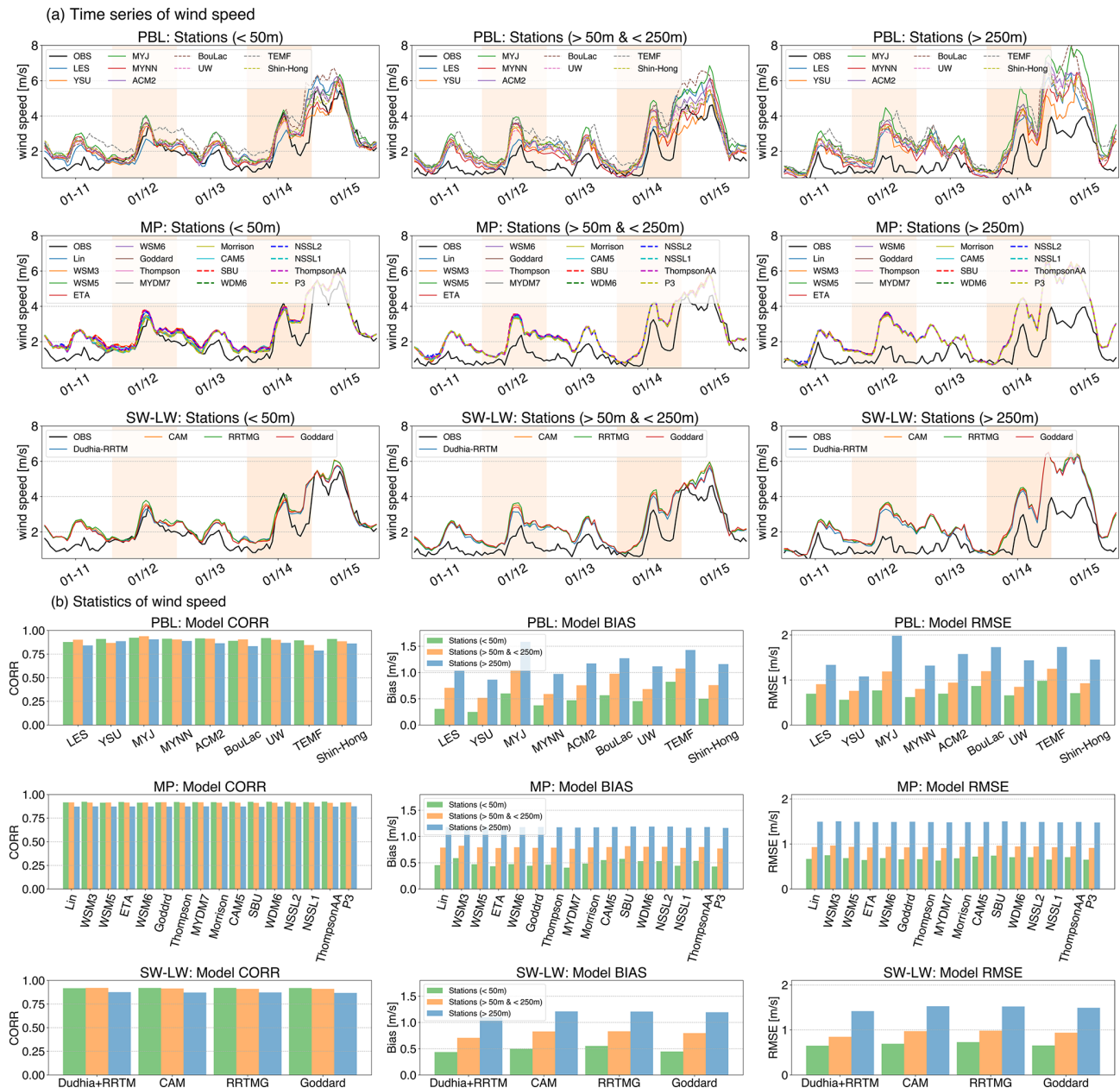
Figure 12. Comparison of simulated wind speeds (m s^{-1}) for stations < 50 m (51 stations in total), > 50, and < 250 (36 stations in total), and > 250 m (19 stations in total) and the corresponding statistic scores.

show smaller differences than that using YSU, and thus the largest differences between YSU and QNSE generally occur at a specific time during the study period, which is also revealed in Fig. 3a.

3.3.3 Impact of land surface models

Figure 15 shows the evaluation of different land surface models (LSMs); only five simulations were conducted using the model configurations with the best Taylor skill score (i.e., YSU in Sect. 3.3.1), and except for the LSM schemes, the

LSMs (i.e., SLAB, NOAH, RUC, and NOAHMP) investigated are listed in Table 3. The simulations reproduce the time series of wind speed well, with a larger spread during 14–15 January 2019. NOAHMP and CLM4 show the best CORR score of 0.93, and NOAH is slightly worse according to this score. Meanwhile, NOAHMP ranks best according to the BIAS and RMSE scores, followed by the RUC scheme. Thus, NOAHMP shows the best performance among different LSMs in wind speed simulations in this study. However, the large difference among LSMs indicates that we should
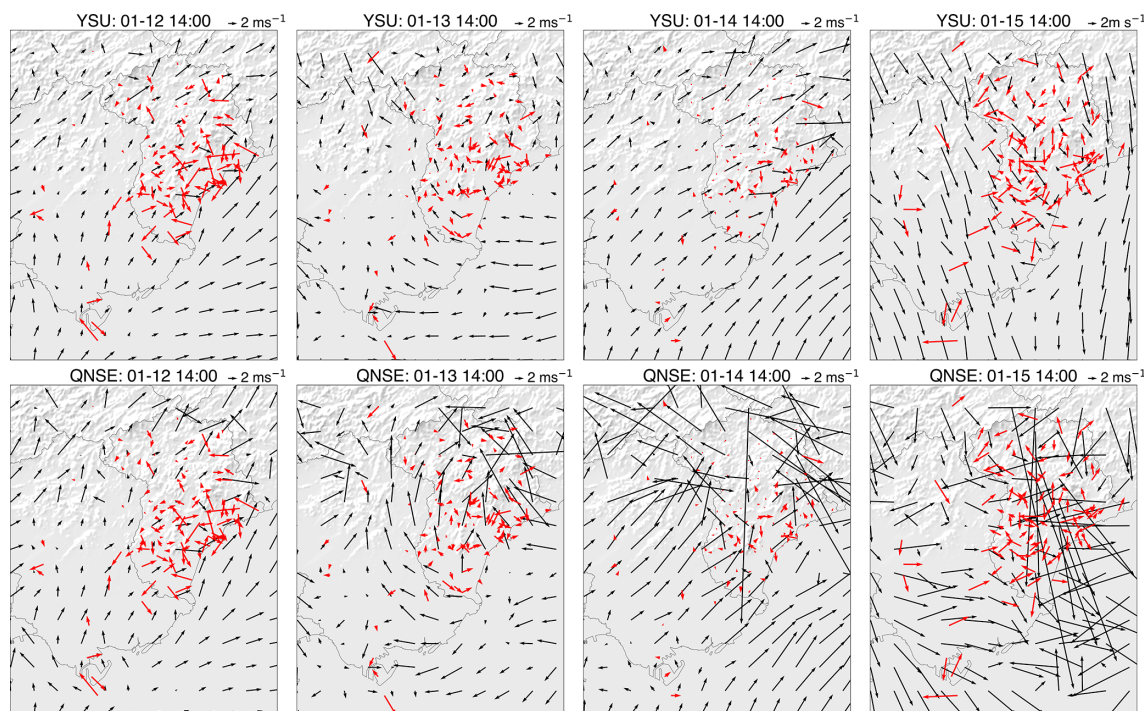
Figure 13. Spatial distribution of simulated (black vector) and observed (red vector) winds at 14:00 LT during the study period from simulations with the YSU and QNSE schemes; the shading indicates the elevation, and the height of the wind is 10 m.

take land surface parameterizations into consideration in future studies.

3.3.4 Impact of surface layer schemes

In the WRF model, the surface layer (SL) schemes are somehow binding with PBL schemes, and it is not possible to run all PBL schemes with the same SL scheme. However, it is meaningful to conduct simulations using a specific PBL scheme that can work with multiple SL schemes to investigate the effect of SL schemes on wind simulation. Figure 16 compares the simulation results of different SL (MM5, Janjic, GFS, MYNN, and PX, Table 4) schemes using UW as the PBL scheme, and the other model configurations are the same as the simulation with the best Taylor skill score. Simulations with different SL schemes generally reproduce the time series of wind speed well, with CORR scores of about 0.93 for most schemes. However, all simulations overestimate the wind speed, especially for the Janjic scheme. At the same time, according to the BIAS and RMSE scores, MYNN shows the best performance, followed by the GFS and PX schemes. Thus, the SL schemes also have a major influence on the wind simulation.

3.3.5 Impact of options in the YSU scheme

The impact of different options in YSU on wind-speed simulation is illustrated in Fig. 17, the simulation with the best Taylor skill score is referred to as YSU, and three extra simulations with top-down mixing option turning off (No_mix), topographic correction with option turning off (No_topo), and both options turning off (No_topo_mix) were conducted for comparison. The simulated wind speed increases when we turn off the individual or both options, which enlarges the overestimation of wind speed under stable conditions in our study (Fig. 15a). Turning off the two options in YSU degrades the model performance with worse evaluation metrics. For example, the BIAS score increases from 0.36 to 0.67 m s^{-1} in No_topo, to 0.43 m s^{-1} in No_mix, and to 0.69 m s^{-1} in the No_topo_mix simulation. At the same time, RMSE scores show similar degradation when turning off the options in YSU.

4 Summary and discussion

In this study, we investigate wind simulations under stable conditions when a haze event affected North China. Surface meteorological observations are used to evaluate the WRF model's ability to reproduce the evolution of winds during the event. The grid spacing of 0.5 km used in this study belongs to the PBL gray zone resolution, which has rarely been used in previous simulation studies in China, and thus the results of this study provide a valuable reference for other simulations over North China. A number of WRF sensitivity experiments (640 in total) are conducted, altering the PBL, MP, and SW–LW schemes to determine the sensitivity of
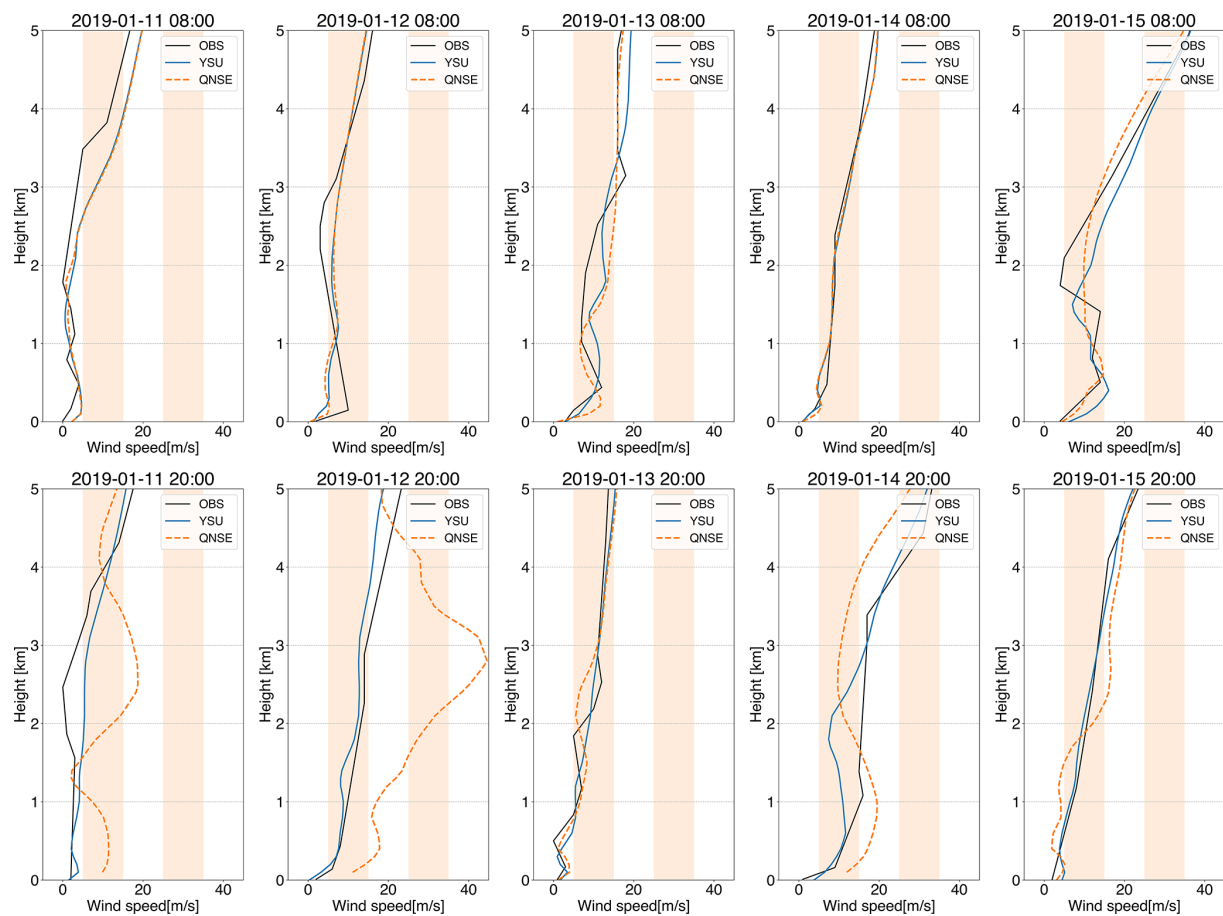
Figure 14. Wind speed profile from observations and simulations with the YSU and QNSE schemes at 08:00 and 20:00 LT during the study period.

Table 3. List of land surface models investigated in this study.

No.	Scheme name	References
1	Five-layer thermal diffusion scheme (SLAB)	Dudhia (1996)
2	NOAH	Chen and Dudhia (2001)
3	Rapid Update Cycle scheme (RUC)	Smirnova et al. (2000)
4	Noah-MP (NOAHMP)	Yang et al. (2011); Niu et al. (2011)
5	Community Land Model Version 4 (CLM4)	Lawrence et al. (2011)

wind speed and direction simulations to model physical parameterizations. Further investigations considering the ocean proximity, elevation, and other model options are conducted to provide deeper insight into the factors that influence model sensitivities.

In general, the WRF model reproduces the temporal variation of wind speed over the study area well, and the spread in wind speed is largest within the PBL schemes tested, followed by SW–LW, and then the MP schemes. The wind direction is notably worse reproduced by WRF compared to wind speed. This result is consistent with the findings of previous simulations performed in other locations (Dzebre

and Adaramola, 2020; Gómez-Navarro et al., 2015; Santos-Alamillos et al., 2013).

Among all PBL schemes, MYJ shows the best CORR score of 0.96, and MYNN, ACM2, and UW are slightly worse according to this score. YSU is the best scheme according to the BIAS and RMSE scores (0.45 and 0.61 m s^{-1}), followed by MYNN (0.55 and 0.70 m s^{-1}). For the SW–LW and MP schemes, the CORR scores are similar, and Dudhia–RRTM and MYDM7 show the best model performances out of all the SW–LW and MP schemes according to the BIAS and RMSE scores. The simulation using the YSU PBL, WDM6 MP and Dudhia–RRTM SW–LW schemes shows the
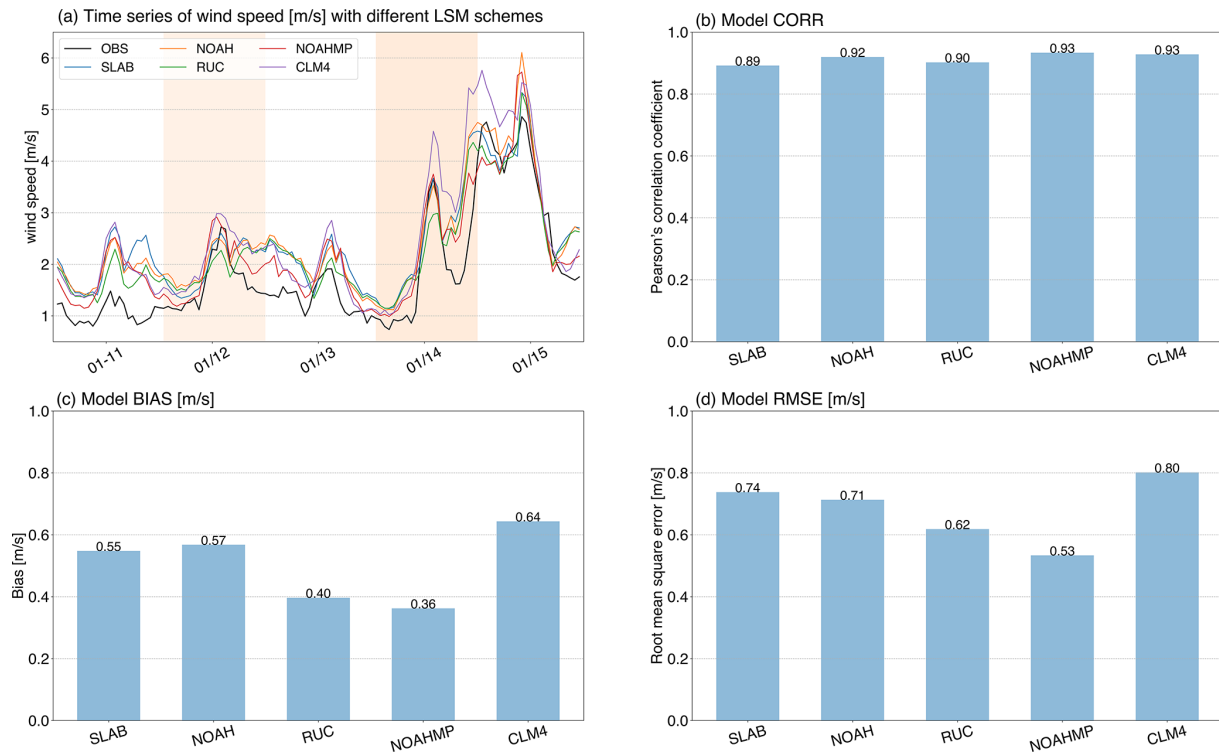
Figure 15. Same as Fig. 3 but for simulations with different land surface schemes. The PBL, MP, and SW–LW schemes used are the same as the simulation with the best Taylor skill score (WDM6 in Fig. 10).
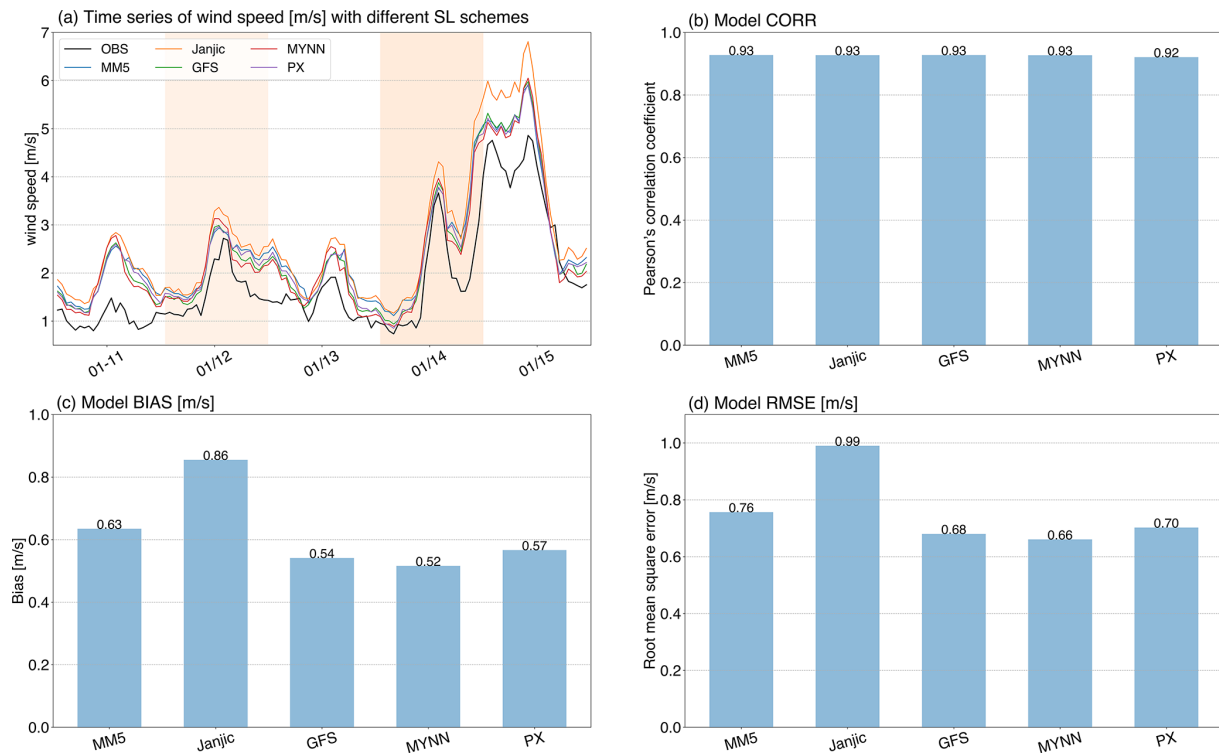

Figure 16. Same as Fig. 3 but for simulations with different surface layer schemes.

Table 4. List of surface schemes investigated in this study.

No.	Scheme name	References
1	Revised MM5 Monin–Obukhov (MM5)	Jiménez et al. (2012)
2	Monin–Obukhov Janjic (Janjic)	Janjić (1994)
3	NCEP Global Forecast System (GFS)	Hong et al. (2004)
4	MYNN surface layer (MYNN)	Nakanishi and Niino (2009)
5	Pleim–Xiu surface layer (PX)	Pleim (2006)
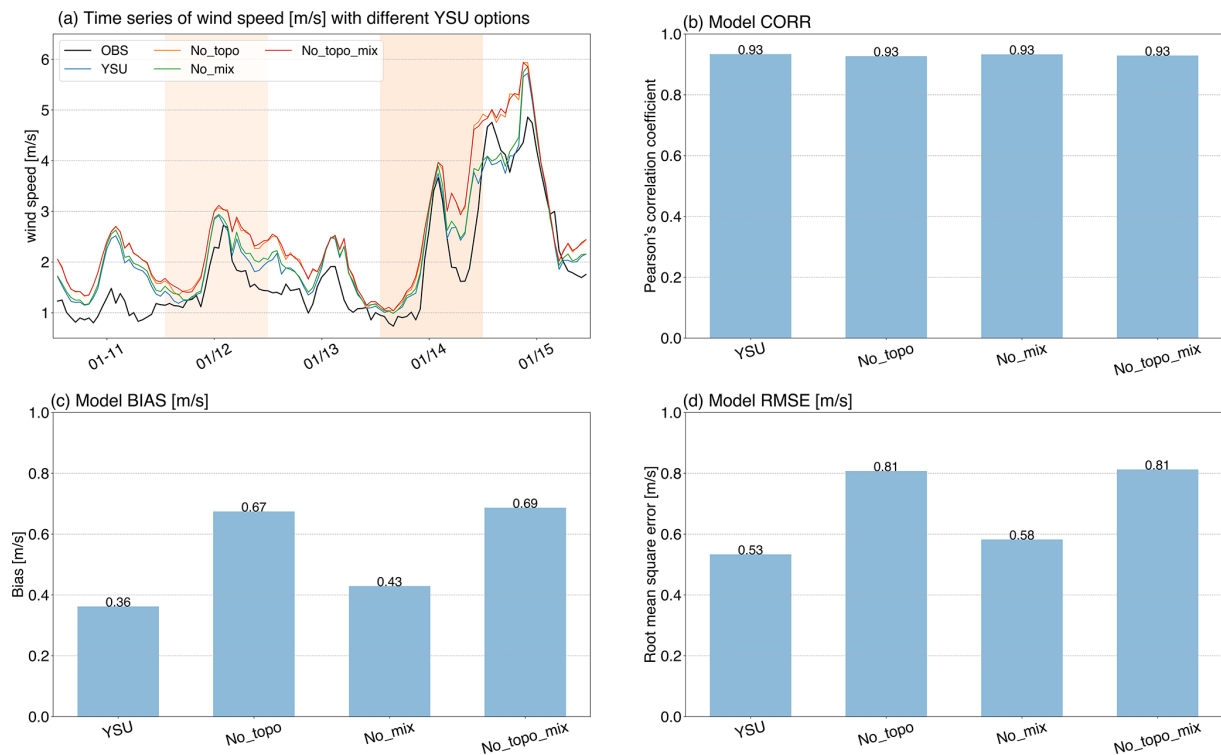
Figure 17. Same as Fig. 3 but for simulations with different YSU options.

best performance, with the highest Taylor skill score. Interactions among the physical parameterization schemes also play an important role in wind simulations, as the best verification scores can be achieved by a certain combination of schemes. The ensemble mean of all the simulations shows the highest CORR core in wind speed, while the 10 best simulations show much better performance than the ensemble in terms of BIAS and RMSE.

The schemes with the best performances for inland stations are consistent with the results of all the stations, as the majority of stations are inland stations; however, for coastal stations, MYNN is the best scheme among all PBL schemes according to CORR, while LES (YSU) shows the best BIAS (RMSE) score. For SW–LW schemes, Goddard schemes show the best scores of CORR, BIAS, and RMSE, while Dudhia–RRTM schemes rank worst according to the CORR score. The schemes with the best performance are similar to different elevations for different parameterization

types; however, model performance tends to degrade with increasing elevation.

As in our study, the model ensemble does not always provide the best performance and model post-processing, and the bias correction techniques are especially needed to be taken into consideration, which can significantly reduce the systematic errors in model simulation. In addition, the PBL schemes play a dominant role in wind simulation, and further tuning of the parameters within the PBL schemes, such as the turbulent kinetic energy (TKE) dissipation rate, TKE diffusion factor, and turbulent length-scale coefficients, is needed. In addition to the PBL and SW–LW schemes, the LSM and SL schemes also have a non-negligible influence on the wind simulation, which should be taken into consideration in future studies. Finally, it is worth pointing out that the presented findings in this study could be unique to the meteorological setup of the event, the location, the input dataset, the

domain setup, and other unchanged parameterization types or model settings.

References

Angevine, W. M., Jiang, H., and Mauritsen, T.: Performance of an eddy diffusivity–mass flux scheme for shallow cumulus boundary layers, Mon. Weather Rev., 138, 2895–2912, 2010.

Barlage, M., Miao, S., and Chen, F.: Impact of physics parameterizations on high-resolution weather prediction over two Chinese megacities, J. Geophys. Res.-Atmos., 121, 4487–4498, 2016.

Bougeault, P. and Lacarrere, P.: Parameterization of orography-induced turbulence in a mesobeta–scale model, Mon. Weather Rev., 117, 1872–1890, 1989.

Bretherton, C. S. and Park, S.: A new moist turbulence parameterization in the Community Atmosphere Model, J. Climate, 22, 3422–3448, 2009.

Cai, W., Li, K., Liao, H., Wang, H., and Wu, L.: Weather conditions conducive to Beijing severe haze more frequent under climate change, Nat. Clim. Change, 7, 257–262, https://doi.org/10.1038/nclimate3249, 2017.

Carvalho, D., Rocha, A., Gómez-Gesteira, M., and Silva Santos, C.: Offshore wind energy resource simulation forced by different reanalyses: Comparison with observed data in the Iberian Peninsula, Appl. Energ., 134, 57–64, https://doi.org/10.1016/j.apenergy.2014.08.018, 2014a.

Carvalho, D., Rocha, A., Gómez-Gesteira, M., and Silva Santos, C.: Sensitivity of the WRF model wind simulation and wind energy production estimates to planetary boundary layer parameterizations for onshore and offshore areas in the Iberian Peninsula, Appl. Energ., 135, 234–246, https://doi.org/10.1016/j.apenergy.2014.08.082, 2014b.

Chang, R., Zhu, R., Badger, M., Hasager, C. B., Xing, X., and Jiang, Y.: Offshore Wind Resources Assessment from Multiple Satellite Data and WRF Modeling over South China Sea, Remote Sens.-Basel, 7, 467–487, 2015.

Chen, F. and Dudhia, J.: Coupling an advanced land-surface hydrology model with the Penn State-NCAR MM5 modeling system. Part I: Model description and implementation, Mon. Weather Rev., 129, 569–585, 2001.

Chen, S. H. and Sun, W. Y.: A one-dimensional time dependent cloud model, J. Meteorol. Soc. Jpn. Ser. II, 80, 99–118, 2002.

Cheng, W. Y. Y., Liu, Y., Liu, Y., Zhang, Y., Mahoney, W. P., and Warner, T. T.: The impact of model physics on numerical wind forecasts, Renew. Energ., 55, 347–356, https://doi.org/10.1016/j.renene.2012.12.041, 2013.

Collins, W. D., Rasch, P. J., Boville, B. A., Hack, J. J., McCaa, J. R., Williamson, D. L., Kiehl, J. T., Briegleb, B., Bitz, C., and Lin, S.-J.: Description of the NCAR community atmosphere model (CAM 3.0), NCAR Tech. Note NCAR/TN-464+ STR, 226, 1326–1334, https://doi.org/10.5065/D63N21CH, 2004.

Deardorff, J.: Sub-grid-scale turbulence modeling, Adv. Geophys., 28, 337–343, https://doi.org/10.1016/S0065-2687(08)60193-4, 1985.

Dudhia, J.: Numerical study of convection observed during the winter monsoon experiment using a mesoscale two-dimensional model, J. Atmos. Sci., 46, 3077–3107, 1989.

Dudhia, J.: A multi-layer soil temperature model for MM5, in: 6th PSU/NCAR Mesoscale Model Users' Workshop, Boulder, CO, 22–24 July 1996, 49–50, 1996.

Dzebre, D. E. K. and Adaramola, M. S.: A preliminary sensitivity study of Planetary Boundary Layer parameterisation schemes in the weather research and forecasting model to

surface winds in coastal Ghana, Renew. Energ., 146, 66–86, https://doi.org/10.1016/j.renene.2019.06.133, 2020.

Eaton, B.: User's guide to the Community Atmosphere Model CAM-5.1, NCAR, http://www.cesm.ucar.edu/models/cesm1.0/cam (last access: 16 September 2020), 2011.

Falasca, S., Gandolfi, I., Argentini, S., Barnaba, F., Casasanta, G., Di Liberto, L., Petenko, I., and Curci, G.: Sensitivity of near-surface meteorology to PBL schemes in WRF simulations in a port-industrial area with complex terrain, Atmos. Res., 264, 105824, https://doi.org/10.1016/j.atmosres.2021.105824, 2021.

Fernández-González, S., Martín, M. L., García-Ortega, E., Merino, A., Lorenzana, J., Sánchez, J. L., Valero, F., and Rodrigo, J. S.: Sensitivity Analysis of the WRF Model: Wind-Resource Assessment for Complex Terrain, J. Appl. Meteorol. Clim., 57, 733–753, 2018.

Gan, Y., Liang, X.-Z., Duan, Q., Chen, F., Li, J., and Zhang, Y.: Assessment and Reduction of the Physical Parameterization Uncertainty for Noah-MP Land Surface Model, Water Resour. Res., 55, 5518–5538, https://doi.org/10.1029/2019WR024814, 2019.

Gao, M., Carmichael, G. R., Wang, Y., Saide, P. E., Yu, M., Xin, J., Liu, Z., and Wang, Z.: Modeling study of the 2010 regional haze event in the North China Plain, Atmos. Chem. Phys., 16, 1673–1691, https://doi.org/10.5194/acp-16-1673-2016, 2016.

Gao, X., Shi, Y., and Giorgi, F.: Comparison of convective parameterizations in RegCM4 experiments over China with CLM as the land surface model, Atmospheric and Oceanic Science Letters, 9, 246–254, https://doi.org/10.1080/16742834.2016.1172938, 2016.

Gholami, S., Ghader, S., Khaleghi-Zavareh, H., and Ghafarian, P.: Sensitivity of WRF-simulated 10 m wind over the Persian Gulf to different boundary conditions and PBL parameterization schemes, Atmos. Res., 247, 105147, https://doi.org/10.1016/j.atmosres.2020.105147, 2021.

Gómez-Navarro, J. J., Raible, C. C., and Dierer, S.: Sensitivity of the WRF model to PBL parametrisations and nesting techniques: evaluation of wind storms over complex terrain, Geosci. Model Dev., 8, 3349–3363, https://doi.org/10.5194/gmd-8-3349-2015, 2015.

Gonçalves-Ageitos, M., Barrera-Escoda, A., Baldasano, J. M., and Cunillera, J.: Modelling wind resources in climate change scenarios in complex terrains, Renew. Energ., 76, 670–678, 2015.

Hersbach, H., Bell, B., Berrisford, P., Biavati, G., Horányi, A., Muñoz Sabater, J., Nicolas, J., Peubey, C., Radu, R., Rozum, I., Schepers, D., Simmons, A., Soci, C., Dee, D., and Thépaut, J.-N.: ERA5 hourly data on pressure levels from 1959 to present, Copernicus Climate Change Service (C3S) Climate Data Store (CDS) [data set], https://doi.org/10.24381/cds.bd0915c6, 2018.

Hersbach, H., Bell, B., Berrisford, P., Hirahara, S., Horányi, A., Muñoz-Sabater, J., Nicolas, J., Peubey, C., Radu, R., Schepers, D., and Simmons, A.: The ERA5 global reanalysis, Q. J. Roy. Meteor. Soc., 146, 1999–2049, 2020.

Hong, S., Noh, Y., and Dudhia, J.: A new vertical diffusion package with an explicit treatment of entrainment processes, Mon. Weather Rev., 134, 2318–2341, 2006.

Hong, S.-Y. and Lim, J.-O. J.: The WRF single-moment 6-class microphysics scheme (WSM6), Asia-Pac. J. Atmos. Sci., 42, 129–151, 2006.

Hong, S.-Y., Dudhia, J., and Chen, S.-H.: A revised approach to ice microphysical processes for the bulk parameterization of clouds and precipitation, Mon. Weather Rev., 132, 103–120, 2004.

Honnert, R., Couvreux, F., Masson, V., and Lancz, D.: Sampling the structure of convective turbulence and implications for grey-zone parametrizations, Bound.-Lay. Meteorol., 160, 133–156, 2016.

Iacono, M. J., Delamere, J. S., Mlawer, E. J., Shephard, M. W., Clough, S. A., and Collins, W. D.: Radiative forcing by long-lived greenhouse gases: Calculations with the AER radiative transfer models, J. Geophys. Res.-Atmos., 113, D13103, https://doi.org/10.1029/2008JD009944, 2008.

Janjić, Z. I.: The step-mountain eta coordinate model: Further developments of the convection, viscous sublayer, and turbulence closure schemes, Mon. Weather Rev., 122, 927–945, 1994.

Jiménez, P. A. and Dudhia, J.: Improving the representation of resolved and unresolved topographic effects on surface wind in the WRF model, J. Appl. Meteorol. Clim., 51, 300–316, 2012.

Jimenez, P. A., Dudhia, J., Fidel Gonzalez–Rouco, J., Navarro, J., Montavez J., and Garcia-Bustamante, E.: A revised scheme for the WRF surface layer formulation, Mon. Weather Rev., 140, 898–918, 2012.

Karlsson, K., Riihelä, A., Trentmann, J., Stengel, M., Meirink, J., Solodovnik, I., Devasthale, A., Manninen, T., Jääskeläinen, E., Anttila, K., Kallio-Myers, V., Benas, N., Selbach, N., Stein, D., Kaiser, J., and Hollmann, R.: ICDR AVHRR-based on CLARA-A2 methods, Satellite Application Facility on Climate Monitoring, https://doi.org/10.5676/EUM_SAF_CM/CLARA_AVHRR/V002_01, 2021.

Kong, X., Wang, A., Bi, X., Sun, B., and Wei, J.: The hourly precipitation frequencies in the tropical-belt version of WRF: sensitivity to cumulus parameterization and radiative schemes, J. Climate, 35, 285–304, 2022.

Lawrence, D., Oleson, K., Flanner, M., Thornton, P., Swenson, S., Lawrence, P., Zeng, X., Yang, Z., Levis, S., Sakaguchi, K., Bonan, G., and Slater, A.: Parameterization improvements and functional and structural advances in Version 4 of the Community Land Model, J. Adv. Model. Earth Sy., 3, M03001, https://doi.org/10.1029/2011MS00045, 2011.

Li, J., Ding, C., Li, F., and Chen, Y.: Effects of single- and double-moment microphysics schemes on the intensity of super typhoon Sarika (2016), Atmos. Res., 238, 104894, https://doi.org/10.1016/j.atmosres.2020.104894, 2020.

Li, M., Tang, G., Huang, J., Liu, Z., An, J., and Wang, Y.: Characteristics of winter atmospheric mixing layer height in Beijing-Tianjin-Hebei region and their relationship with the atmospheric pollution, Environm. Sci., 36, 1935–1943, https://doi.org/10.13227/j.hjkx.2015.06.004, 2015 (in Chinese).

Li, S., Sun, X., Zhang, S., Zhao, S., and Zhang, R.: A Study on Microscale Wind Simulations with a Coupled WRF–CFD Model in the Chongli Mountain Region of Hebei Province, China, Atmosphere-Basel, 10, 731, 2019.

Lim, K.-S. S. and Hong, S.-Y.: Development of an effective double-moment cloud microphysics scheme with prognostic cloud condensation nuclei (CCN) for weather and climate models, Mon. Weather Rev., 138, 1587–1612, 2010.

Lin, Y. and Colle, B. A.: A new bulk microphysical scheme that includes riming intensity and temperature-dependent ice characteristics, Mon. Weather Rev., 139, 1013–1035, 2011.

Mansell, E. R., Ziegler, C. L., and Bruning, E. C.: Simulated electrification of a small thunderstorm with two-moment bulk microphysics, J. Atmos. Sci., 67, 171–194, 2010.

Matsui, T., Zhang, S. Q., Lang, S. E., Tao, W.-K., Ichoku, C., and Peters-Lidard, C. D.: Impact of radiation frequency, precipitation radiative forcing, and radiation column aggregation on convection-permitting West African monsoon simulations, Clim. Dynam., 55, 193–213, 2020.

Mesinger, F.: Forecasting upper tropospheric turbulence within the framework of the Mellor-Yamada 2.5 closure, Res. Activ. Atmos. Oceanic Mod., CAS/JSC WGNE Reper No. 18, WMO, Geneva, 28–24, 1993.

Milbrandt, J. and Yau, M.: A multimoment bulk microphysics parameterization. Part I: Analysis of the role of the spectral shape parameter, J. Atmos. Sci., 62, 3051–3064, 2005.

Mirocha, J., Lundquist, J., and Kosović, B.: Implementation of a nonlinear subfilter turbulence stress model for large-eddy simulation in the Advanced Research WRF model, Mon. Weather Rev., 138, 4212–4228, 2010.

Mlawer, E. J., Taubman, S. J., Brown, P. D., Iacono, M. J., and Clough, S. A.: Radiative transfer for inhomogeneous atmospheres: RRTM, a validated correlated-k model for the longwave, J. Geophys. Res.-Atmos., 102, 16663–16682, 1997.

Morrison, H. and Milbrandt, J. A.: Parameterization of cloud microphysics based on the prediction of bulk ice particle properties. Part I: Scheme description and idealized tests, J. Atmos. Sci., 72, 287–311, 2015.

Morrison, H., Thompson, G., and Tatarskii, V.: Impact of cloud microphysics on the development of trailing stratiform precipitation in a simulated squall line: Comparison of one-and two-moment schemes, Mon. Weather Rev., 137, 991–1007, 2009.

Nakanishi, M. and Niino, H.: Development of an improved turbulence closure model for the atmospheric boundary layer, J. Meteorol. Soc. Jpn. Ser. II, 87, 895–912, 2009.

Niu, G.-Y., Yang, Z.-L., Mitchell, K. E., Chen, F., Ek, M. B., Barlage, M., Kumar, A., Manning, K., Niyogi, D., Rosero, E., Tewari, M., and Xia, Y.: The community Noah land surface model with multiparameterization options (Noah-MP): 1. Model description and evaluation with local-scale measurements, J. Geophys. Res.-Atmos., 116, D12109, https://doi.org/10.1029/2010JD015139, 2011.

Pan, L., Liu, Y., Roux, G., Cheng, W., Liu, Y., Hu, J., Jin, S., Feng, S., Du, J., and Peng, L.: Seasonal variation of the surface wind forecast performance of the high-resolution WRF-RTFDDA system over China, Atmos. Res., 259, 105673, https://doi.org/10.1016/j.atmosres.2021.105673, 2021.

Pleim, J. E.: A simple, efficient solution of flux-profile relationships in the atmospheric surface layer, J. Appl. Meteorol. Clim., 45, 341–347, 2006.

Pleim, J. E.: A combined local and nonlocal closure model for the atmospheric boundary layer. Part I: Model description and testing, J. Appl. Meteorol. Clim., 46, 1383–1395, 2007.

Prieto-Herráez, D., Frías-Paredes, L., Cascón, J. M., Lagüela-López, S., Gastón-Romeo, M., Asensio-Sevilla, M. I., Martín-Nieto, I., Fernandes-Correia, P. M., Laiz-Alonso, P., Carrasco-Díaz, O. F., Sáez-Blázquez, C., Hernández, E., Ferragut-Canals, L., and González-Aguilera, D.: Local wind speed forecasting based on WRF-HDWind coupling, Atmos. Res., 248, 105219, https://doi.org/10.1016/j.atmosres.2020.105219, 2021.

Puliafito, S. E., Allende, D. G., Mulena, C. G., Cremades, P., and Lakkis, S. G.: Evaluation of the WRF model configuration for Zonda wind events in a complex terrain, Atmos. Res., 166, 24–32, https://doi.org/10.1016/j.atmosres.2015.06.011, 2015.

Rajeevan, M., Kesarkar, A., Thampi, S. B., Rao, T. N., Radhakrishna, B., and Rajasekhar, M.: Sensitivity of WRF cloud microphysics to simulations of a severe thunderstorm event over Southeast India, Ann. Geophys., 28, 603–619, https://doi.org/10.5194/angeo-28-603-2010, 2010.

Rogers, E., Black, T., Ferrier, B., Lin, Y., Parrish, D., and DiMego, G.: Changes to the NCEP Meso Eta Analysis and Forecast System: Increase in resolution, new cloud microphysics, modified precipitation assimilation, modified 3DVAR analysis, NWS Technical Procedures Bulletin, 488, 15, 2001.

Rybchuk, A., Optis, M., Lundquist, J. K., Rossol, M., and Musial, W.: A Twenty-Year Analysis of Winds in California for Offshore Wind Energy Production Using WRF v4.1.2, Geosci. Model Dev. Discuss. [preprint], https://doi.org/10.5194/gmd-2021-50, 2021.

Santos-Alamillos, F. J., Pozo-Vázquez, D., Ruiz-Arias, J. A., Lara-Fanego, V., and Tovar-Pescador, J.: Analysis of WRF Model Wind Estimate Sensitivity to Physics Parameterization Choice and Terrain Representation in Andalusia (Southern Spain), J. Appl. Meteorol. Clim., 52, 1592–1609, https://doi.org/10.1175/jamc-d-12-0204.1, 2013.

Shin, H. H. and Hong, S.: Representation of the subgrid-scale turbulent transport in convective boundary layers at gray-zone resolutions, Mon. Weather Rev., 143, 250–271, 2015.

Skamarock, W. C., Klemp, J. B., Dudhia, J., Gill, D. O., Barker, D., Duda, M. G., Huang, X. Y., Wang W., and Powers, J. G.: A description of the Advanced Research WRF version 3, NCAR Technical note-475+ STR, https://doi.org/10.5065/D68S4MVH, 2008 (data available at https://www2.mmm.ucar.edu/wrf/users/download/get_source.html, last access: 21 July 2021).

Smirnova, T. G., Brown, J. M., Benjamin, S. G., and Kim, D.: Parameterization of cold-season processes in the MAPS land surface scheme, J. Geophys. Res., 105, 4077–4086, https://doi.org/10.1029/1999JD901047, 2000.

Song, M., Wu, J., Song, M., Zhang, L., and Zhu, Y.: Spatiotemporal regularity and spillover effects of carbon emission intensity in China's Bohai Economic Rim, Sci. Total Environ., 740, 140184, https://doi.org/10.1016/j.scitotenv.2020.140184, 2020.

Stegehuis, A. I., Vautard, R., Ciais, P., Teuling, A. J., Miralles, D. G., and Wild, M.: An observation-constrained multi-physics WRF ensemble for simulating European mega heat waves, Geosci. Model Dev., 8, 2285–2298, https://doi.org/10.5194/gmd-8-2285-2015, 2015.

Sukoriansky, S., Galperin, B., and Perov, V.: Application of a new spectral theory of stably stratified turbulence to the atmospheric boundary layer over sea ice, Bound.-Lay. Meteorol., 117, 231–257, 2005.

Tao, W.-K., Simpson, J., and McCumber, M.: An ice-water saturation adjustment, Mon. Weather Rev., 117, 231–235, 1989.

Taraphdar, S., Pauluis, O. M., Xue, L., Liu, C., Rasmussen, R., Ajayamohan, R. S., Tessendorf, S., Jing, X., Chen, S., and Grabowski, W. W.: WRF Gray-Zone Simulations of Precipitation Over the Middle-East and the UAE: Impacts of Physical Parameterizations and Resolution, J. Geophys. Res.-Atmos., 126, e2021JD034648, https://doi.org/10.1029/2021JD034648, 2021.

Thompson, G. and Eidhammer, T.: A study of aerosol impacts on clouds and precipitation development in a large winter cyclone, J. Atmos. Sci., 71, 3636–3658, 2014.

Thompson, G., Field, P. R., Rasmussen, R. M., and Hall, W. D.: Explicit forecasts of winter precipitation using an improved bulk microphysics scheme. Part II: Implementation of a new snow parameterization, Mon. Weather Rev., 136, 5095–5115, 2008.

Tiedtke, M.: A comprehensive mass flux scheme for cumulus parameterization in large–scale models, Mon. Weather Rev., 117, 1779–1800, 1989.

Ulpiani, G.: On the linkage between urban heat island and urban pollution island: Three-decade literature review towards a conceptual framework, Sci. Total Environ., 751, 141727, https://doi.org/10.1016/j.scitotenv.2020.141727, 2021.

Wang, H., Yu, E., and Yang, S.: An exceptionally heavy snowfall in Northeast china: large-scale circulation anomalies and hindcast of the NCAR WRF model, Meteorol. Atmos. Phys., 113, 11–25, https://doi.org/10.1007/s00703-011-0147-7, 2011.

Wang, T., Zhang, M., and Han, X.: Source Apportionment of $PM_{2.5}$ during a Heavy Pollution Episode in Qinhuangdao in Winter 2019 Using a Chemical Transport Model, Climatic and Environmental Research, 26, 471–481, 2021 (in Chinese).

Wang, X. and Mauzerall, D. L.: Evaluating impacts of air pollution in China on public health: Implications for future air pollution and energy policies, Atmos. Environ., 40, 1706–1721, https://doi.org/10.1016/j.atmosenv.2005.10.066, 2006.

Xia, G., Zhou, L., Minder, J. R., Fovell, R. G., and Jimenez, P. A.: Simulating impacts of real-world wind farms on land surface temperature using the WRF model: physical mechanisms, Clim. Dynam., 53, 1723–1739, https://doi.org/10.1007/s00382-019-04725-0, 2019.

Yang, B., Qian, Y., Berg, L. K., Ma, P.-L., Wharton, S., Bulaevskaya, V., Yan, H., Hou, Z., and Shaw, W. J.: Sensitivity of Turbine-Height Wind Speeds to Parameters in Planetary Boundary-Layer and Surface-Layer Schemes in the Weather Research and Forecasting Model, Bound.-Lay. Meteorol., 162, 117–142, https://doi.org/10.1007/s10546-016-0185-2, 2017.

Yang, Z.-L., Niu, G.-Y., Mitchell, K. E., Chen, F., Ek, M. B., Barlage, M., Longuevergne, L., Manning, K., Niyogi, D., Tewari, M., and Xia, Y.: The community Noah land surface model with multiparameterization options (Noah-MP): 2. Evaluation over global river basins, J. Geophys. Res.-Atmos., 116, D12110, https://doi.org/10.1029/2010JD015140, 2011.

Yu, E., Wang, H., Gao, Y., and Sun, J.: Impacts of cumulus convective parameterization schemes on summer monsoon precipitation simulation over China, Acta Meteorol. Sin., 25, 581–592, 2011.

Yu, E., Wang, H., Sun, J., and Gao, Y.: Climatic response to changes in vegetation in the Northwest Hetao Plain as simulated by the WRF model, Int. J. Climatol., 33, 1470–1481, 2013.

Yu, E., Bai, R., Chen, X., and Shao, L.: Impact of physical parameterizations on wind simulation with WRF V3.9.1.1 under stable conditions at PBL gray-zone resolution: a case study over the coastal regions of North China, Zenodo [data set], https://doi.org/10.5281/zenodo.6505423, 2022.

Zhang, L., Wang, T., Lv, M., and Zhang, Q.: On the severe haze in Beijing during January 2013: Unraveling the effects of meteorological anomalies with WRF-Chem, Atmos. Environ., 104, 11–21, https://doi.org/10.1016/j.atmosenv.2015.01.001, 2015.

Zhang, R., Li, Q., and Zhang, R.: Meteorological conditions for the persistent severe fog and haze event over eastern China in January 2013, Sci. China Earth Sci., 57, 26–35, https://doi.org/10.1007/s11430-013-4774-3, 2014.

Zhao, J., Guo, Z., Su, Z., Zhao, Z., Xiao, X., and Liu, F.: An improved multi-step forecasting model based on WRF ensembles and creative fuzzy systems for wind speed, Appl. Energ., 162, 808–826, 2016.

Zhao, Y., Zhou, J., Fan, Y., Feng, M., and Zhang, Z.: Economic and environmental impacts of China's imported iron ore transport chain under road-to-rail policy: an empirical analysis based on the Bohai Economic Rim, Carbon Manag., 11, 653–671, 2020.

Zhou, X., Yang, K., Beljaars, A., Li, H., Lin, C., Huang, B., and Wang, Y.: Dynamical impact of parameterized turbulent orographic form drag on the simulation of winter precipitation over the western Tibetan Plateau, Clim. Dynam., 53, 707–720, https://doi.org/10.1007/s00382-019-04628-0, 2019.